



저작자표시-비영리-변경금지 2.0 대한민국

이용자는 아래의 조건을 따르는 경우에 한하여 자유롭게

- 이 저작물을 복제, 배포, 전송, 전시, 공연 및 방송할 수 있습니다.

다음과 같은 조건을 따라야 합니다:



저작자표시. 귀하는 원저작자를 표시하여야 합니다.



비영리. 귀하는 이 저작물을 영리 목적으로 이용할 수 없습니다.



변경금지. 귀하는 이 저작물을 개작, 변형 또는 가공할 수 없습니다.

- 귀하는, 이 저작물의 재이용이나 배포의 경우, 이 저작물에 적용된 이용허락조건을 명확하게 나타내어야 합니다.
- 저작권자로부터 별도의 허가를 받으면 이러한 조건들은 적용되지 않습니다.

저작권법에 따른 이용자의 권리는 위의 내용에 의하여 영향을 받지 않습니다.

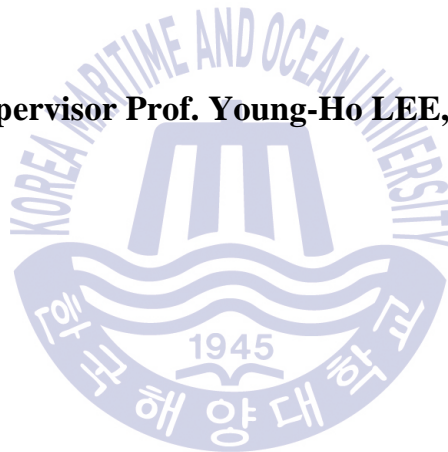
이것은 [이용허락규약\(Legal Code\)](#)을 이해하기 쉽게 요약한 것입니다.

[Disclaimer](#)

Master's Thesis

**A study on the performance of a cross-flow
air turbine utilizing an orifice for OWC
wave energy converters**

Supervisor Prof. Young-Ho LEE, Ph.D



February 2017

**Department of Mechanical Engineering
Graduate School of Korea Maritime and Ocean University**

Hong Goo Kang

본 논문을 강홍구의 공학석사 학위논문으로 인준함

위원장 : 윤형기

위원 : 황태규

위원 : 이영호



2016년 12월 19일

한국해양대학교 일반대학원

Contents

List of Tables	iii
List Figures	iv
Abstract	vii
Nomenclature	ix
Chapter 1. Introduction	1
1.1 Background	1
1.2 Wave Energy Converter	2
1.3 Literature Survey	4
1.3.1 OWC	4
1.3.2 Air turbine for OWC WEC	5
1.3.3 Linear wave theory	7
1.4 Objective of research	12
Chapter 2. CFD analysis of a cross-flow air turbine	14
2.1 ANSYS CFD Code	14
2.1.1 Discretization of the governing equations	14
2.1.2 Turbulence model	16
2.2 Design of cross-flow turbine	19
2.3 Steady State simulation	20
2.3.1 Numerical analysis setup	21
2.3.2 CFD result and discussion.....	23

2.4	Transient simulation	28
2.4.1	Numerical setup	29
2.4.2	Data analysis	30
2.4.3	CFD result and discussion.....	35
Chapter 3.	Validation of an Orifice for turbine damping effects.....	47
3.1	Ideal Air.....	47
3.2	Orifice PTO system	48
3.3	Design of Orifice	49
3.4	Numerical analysis of Orifice.....	50
3.4.1	Numerical analysis setup	50
3.4.2	CFD result and discussion.....	52
3.5	Experimental analysis of Orifice	55
3.6	Result of experiment and comparative study	58
Chapter 4.	Conclusion.....	62
	Acknowledgements.....	64
	Reference.....	65

List of Tables

Table 1 Worldwide wave power installed capacity [4].....	2
Table 2 Selection of WEC Device developers [5]	3
Table 3 Summary of linear (Airy) wave theory characteristics [21]	12
Table 4 Overview of turbulent flow simulation methods [22].....	17
Table 5 Design parameters for the cross-flow air turbine.....	20
Table 6 Boundary condition of CFX pre setup for the cross-flow air turbine in steady state simulation	23
Table 7 Boundary condition of CFX pre setup for the cross-flow air turbine in transient simulation	30
Table 8 Summary of performance of the model scaled cross-flow air turbine by CFD	46
Table 9 Diameter ratio of test orifice plates.....	50

List Figures

Figure 1 Oscillating water column WEC [7]	4
Figure 2 Definition sketch for dimensional linear wave theory (LWT) boundary value [19]	8
Figure 3 Nomenclature of a linear water wave, having a sinusoidal profile [20]...	10
Figure 4 Properties of waves under several depth conditions: (a) deep water, (b) intermediate water, (c) shallow water [20]	11
Figure 5 Configuration of control volume definition (a) and mesh element (b) [22]	14
Figure 6 Configuration of cross-flow air turbine	20
Figure 7 Meshing of the cross-flow air turbine by ICEM CFD	22
Figure 8 Configuration of CFX pre setup domain for the cross-flow air turbine in steady state	22
Figure 9 Schematic configuration of the cross-flow air turbine with division of runner flow passage	24
Figure 10 Velocity vectors in the flow field of the turbine domain at 32rpm rotational speed and 7m/s inlet velocity	25
Figure 11 Pressure contours in the flow field of the turbine domain at 32rpm rotational speed and 7m/s inlet velocity	25
Figure 12 Performance of the cross-flow air turbine by dimensionless analysis....	28
Figure 13 Configuration of CFX pre setup domain for the cross-flow air turbine in transient simulation	29

Figure 14 Visual configuration of the division of time series data into segments for phase averaging [25] 31

Figure 15 Representation of times series cycles for (a) pressure gap between upstream and downstream and (b) flow rate through the turbine in one segment by phase averaging (T=1.5sec) 33

Figure 16 Phase-averaged profile of (a) pressure gap and (b) flow rate (T=1.25sec) 34

Figure 17 Velocity vectors in the flow field of the turbine domain at 1000rpm rotational speed and 2 sec period 36

Figure 18 Pressure contours in the flow field of the turbine domain at 1000rpm rotational speed and 2 sec period 37

Figure 19 Power distribution on entire rotor at different wave periods..... 40

Figure 20 Pressure against flow rate with phase averaging at 1000rpm rotational speed..... 42

Figure 21 Representation of phase averaged times series cycles for turbine torque in one segment..... 44

Figure 22 Phase averaged shaft power and air power..... 46

Figure 23 Meshing of the orifice plate by ICEM CFD 51

Figure 24 Configuration of CFX pre setup domain for the orifice plate in transient simulation..... 51

Figure 25 Phase averaged pressure drop and flow rate diagram of the orifice plates with the turbine result 54

Figure 26 Configuration of OWC chamber with orifice plates 56

Figure 27 Configuration of experimental setup in wave tank..... 57

Figure 28 Experimental setup with OWC chamber in wave tank..... 57

Figure 29 Experimental equipment in OWC chamber for measurement..... 58

Figure 30 Validations of orifice plate as substitute for the cross-flow air turbine between CFD and experiment result..... 61



A study on the performance of a cross-flow air turbine utilizing an orifice for OWC wave energy converters

Hong Goo Kang

Department of Mechanical Engineering

Graduate School of Korea Maritime and Ocean University

Abstract

Ocean energy which includes tidal energy, ocean thermal energy conversion, wave energy and other marine energy currents, hold an enormous amount of untapped energy that, if exploited extensively, have a potential for contributing significantly to the electricity supply of countries facing the sea. One of the most successful and most extensively investigated devices for extracting wave energy is the Oscillating Water Column (OWC). OWCs have been widely developed due to its potential deployment in various water conditions and its simplicity in design. The common OWC wave energy converter consists of fixed or floating structure, which opens to the sea below the water surface and absorbs wave energy, and a turbine coupled to a generator. Wave motion inside the chamber induces an exhalation and inhalation of the trapped air which drive the bi-directional turbine at the opening of the device. The turbine is connected to a generator so that mechanical motion from the rotating blade is converted to an electrical energy.

A cross-flow air turbine is a candidate for use of a self-starting turbine due to its characteristic, high coefficient at a low tip speed ratio. In addition, it has excellent stability

and low noise. With its characteristics this turbine may be more suitable at places where require low noise compared to typical commercialized air turbines such as Wells and impulse turbine. In this research, the investigation of cross-flow air turbine for OWC wave energy converter have been undertaken. First, a numerical analysis of the turbine by CFD have been conducted in order to acquire its performance characteristics in various range of the flow rate with different rotational speed of the rotor. Model scale analysis was proposed to design and compare with experimental model, and 1/16 model scale was determined. In addition, the orifice plate as substitute was adopted not only to simulate the behavior of the turbine by numerical analysis and experiment but also to verify the CFD result with the experiment result. The size of the orifice plate was determined by matching the pressure drop between upstream and downstream of turbine and orifice. Thus, the comparative study between orifice plates and turbine simulation have been proposed.

Key words: Wave energy, OWC, cross-flow air turbine, Orifice, PTO system

Nomenclature

c	Wave phase velocity	m/s^2
g	Gravity acceleration	m/s^2
H	Wave height	m
h	Water depth	m
k	Wave number	-
N	Rotational speed of rotor	rpm
p	pressure	Pa
Q	Flow rate	kg/s
T	Wave period	sec
u	Horizontal wave particle velocity	m/s^2
w	Vertical wave particle velocity	m/s^2
z	Height based on reference	m
α	Angle of attack	$^\circ$
α'	Nozzle tip angle	$^\circ$
β_1	Blade inlet angle	$^\circ$
β_2	Blade outlet angle	$^\circ$
δ	Nozzle entry angle	$^\circ$
f	Wave frequency	Hz
λ	Wave length	m
ρ	Specific fluid density	kg/m^3
ω	Circular wave frequency	rad/sec
ξ	Water particle displacements	kg

Chapter 1. Introduction

1.1 Background

Ocean energy which includes tidal energy, ocean thermal energy conversion, wave energy and other energy currents, hold an enormous amount of untapped energy that, if exploited extensively, have a potential for contributing significantly to the electricity supply of countries facing the sea. The most commercially viable form of resources researched so far are ocean currents and waves which are both on the progress of developing [1]. It is estimated that the total amount of marine and tidal currents energy contain about 5TW [2], the scale of the global total power consumption. In addition, approximately 8,000 to 80,000 TWh/yr of wave energy can be obtained theoretically which provide 15 to 20 times more viable energy per square meter than other type of renewable energy such as solar and wind [3].

A variety of countries are working on research and development of marine energy in open sea test sites by building the infrastructure, capability, and strategic partnerships to support the private sector on the path to commercialization. It is seen that building and developing sea testing facilities for different steps of the development process is a valuable measure at governmental level. These infrastructure promotes the development of ocean energy by allowing practical experience of installation, decommissioning, operation, maintenance activities for full scale prototypes and farms, as well as on streamlining procedures and services [4].

Work of several marine energy including wave energy infrastructures are currently on progress in worldwide. Various technologies in terms of marine energy are on the stage of testing and deploying in open sea. Table 1 presents the approximate amount of global ocean wave power installed capacity. UK have the largest amount of installed capacity in wave energy as 960 kW, and other European countries have a plan to build huge amount of capacity.

Table 1 Worldwide wave power installed capacity [4]

Countries	Installed capacity [kW]	Consented projects [kW]
Portugal	400	5000
UK	960	40000
Canada	9	-
USA	-	1545
Spain	296	-
Sweden	200	10400-10600
Denmark	-	50
Belgium	-	Up to 20000
Norway	200	-
China	450	2760
Republic of Korea	500	500

1.2 Wave Energy Converter

Currently, wave energy converters are in the research and development stage of technology development. Although there are certain device developers who have had a grid connected device for last decades, the sector as a whole have no commercially available production wave devices. Over 100 concepts of device development have taken place in over 30 countries across the world. Various testing facilities have increased the availability of allowing concepts of wave energy conversion to be

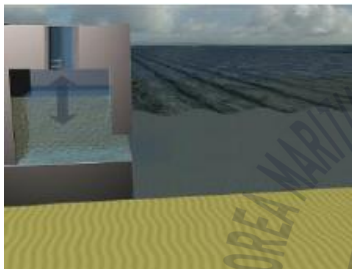
tested with the grid connected berths. Certain developed devices have had several months of at-sea testing, and some of devices are nearing on the commercially viable phase [5]. A summary of device developers within each of the technology types is illustrated in Table 2.

Table 2 Selection of WEC Device developers [5]

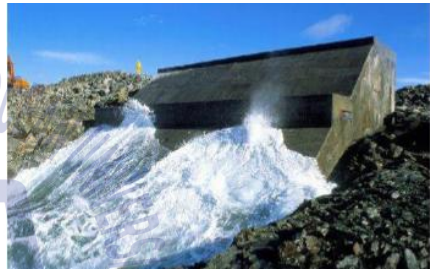
Device Type	Classification (Wave)	Device Developers at Various Stages of Development
Attenuator	A	Pelamis, Dexa-wave, Alba TERN
Point Absorber	B	Ocean Power Technologies, Wavestar, Seatricity, CETO Wave Energy Technology, SeaRaser, SeaNergy
Oscillating Wave Surge Converter (OWSC)	C	Aquamarine Power, Waveroller, Langlee Wave Power
Oscillating Water Column (OWC)	D	Voith Hydro WaveGen, WaveEC Pico Plant, Oceanlinx, Ocean Energy
Overtopping/ Terminator	E	Wave Dragon, Waveplane
Pressure Differential	F	AWS Ocean Energy
Rotating Mass	G	Wello Oy
Bulge Wave	H	Checkmate Seaenergy

Oscillating water column (OWC) device as shown in Figure 1 (a) consists of a chamber structure and turbine, connected to a generator. The device operates by wave energy which makes the free surface of the ocean fluid in the chamber to oscillate and causes a changing in air pressure within the chamber driving the volume of air through the bi-directional turbine at the opening of the device. The turbine is connected to a generator so that mechanical motion from the turbine provides the production of electrical energy. This device is typically installed near shore bottom

as a bottom mounted structure, covered within an artificial breakwater, or moored in deep offshore as a floating platform. Voith Wavegen has successfully developed several OWC projects, and Figure 1 (b) represents one of OWC devices, called LIMPET (Land Installed Marine Powered Energy Transformer). The device is a shoreline based oscillating water column energy converter, and it consists of 16 individual OWC wave energy units, covered by a 100m section of the breakwater [6].



(a) Oscillating water column WEC [7]



(b) Voith Wavegen [8]

Figure 1 Oscillating water column WEC [7]

1.3 Literature Survey

1.3.1 OWC

The first concept of OWC wave energy converter was proposed and tested by Miyazaki and Masuda in 1979 [9], and it was subsequently investigated by an experimentation through field test [10]. In recent, the research of OWC device have been gradually increased and several commercial-level OWC plants have been installed and successfully operated due to its various advantages over other wave energy converters in terms of (i) a confirmed design; some practical bottom fixed OWC plants have been constructed and operated to generate electricity to the grids for many years, (ii) a relatively high wave-to-wire efficiency including high primary

converting efficiency and high reliability of mechanical power converting efficiency, (iii) free corrosion of core component due to sea water, and (iv) a lower force and a higher speed for a certain PTO which induce a high reliability of the PTO system [11].

For analysis, one of the significant consideration for the OWC wave devices is the air compressibility in the section of air chamber due to its large volumetric space and high air chamber pressure in the typical OWC devices. Sarmiento et al. [12] have introduced a linearized formula in terms of the flow rate through the PTO system, based on the assumption of an isentropic flow. Sheng et al. [13] have researched the air compressibility by formulating a full thermodynamic differential equation for the volumetric flow rate through the PTO system and in the chamber as well, and the validation of the proposed method has been processed using experimental data [14]. With the calibrated relationship between the flow rate and pressure through the PTO system, the complicated analysis of the PTO process could be simplified. Thus, it induces the simplified calculation of the power conversion process from the PTO. In this research, the simplified formula of the relation between the pressure and flow rate through the PTO system have been adopted.

1.3.2 AIR TURBINE FOR OWC WEC

The cross-flow turbine was first invented and developed by the Australian engineer, A.G.M Mitchell in 1903, and its further development was processed by the Hungarian Prof. Donat Banki in Germany [15]. The main characteristic of the cross-flow turbine is its relatively wide range of operating range from low to medium head. In addition, its main advantage is that the turbine provide the similar performance

and efficiency for different flow rates. However, the cross-flow type turbine have normally been applied as a water turbine in hydropower system rather than as air turbines in wave energy converters. Only a few studies have handled with the cross-flow turbine for the self-rectifying air turbines which can be used for wave energy conversion. Mockmore and Merryfield [16] introduced the design theory of the cross-flow turbine with all design factors such as blade angle, spacing and number according to different flow conditions. Fukutomi et al. [17] conducted the numerical calculation and experiment of the flow through the cross-flow turbine nozzle and provided the design parameters for the shape of nozzle, and its significant design parameters are nozzle entry arc, throat width and upper wall shape. One research of the self-rectifying cross-flow air turbine for wave energy conversion was induced by Akabane et al. [18]. The test performed under steady flow conditions with three kinds of turbine having 30 blades, 200mm diameter and 100mm width that produced the maximum efficiency as 29%. Although the result seems that the turbine is inferior to other types of air turbines such as Wells and Impulse turbine, it is inappropriate to compared the single cross-flow turbine to the other turbines having extra installations such as guide vanes which increase the its performance. The cross-flow air turbine have a potential to be more suitable for OWC wave energy converter with its benefits, wide range of operating range with relatively constant performance. Thus, in this research, the investigation of the cross-flow air turbine for OWC wave energy converter have been conducted.

1.3.3 LINEAR WAVE THEORY

Linear wave theory (LWT) is the most generally applied description for wind-generated surface gravity waves. Assumption in LWT is that the wave height, H , is relatively small compared to the wavelength, λ (small amplitude assumption, $H/2\lambda$), and the water depth, h , is not small compared to wavelength (finite depth assumption, h/λ). Linear wave theory, in spite of the restriction of the small amplitude ratio $H/2\lambda \ll 1$, allows a reasonably proper estimate of both dynamic and kinematic wave fields even when the small amplitude restriction is not valid.

The unknowns of fundamental fluid for an incompressible fluid are the Eulerian fields of the velocity $\vec{q}(x, z, t)$ that is a vector with a scalar vertical component $w(x, z, t)$ and horizontal component $u(x, z, t)$ given [19] by

$$\vec{q}(x, z, t) = u(x, z, t)\vec{e}_x + w(x, z, t)\vec{e}_z, \quad (1.1)$$

where \vec{e}_x and \vec{e}_z are unit vectors in the x and z coordinates axis respectively, and the total pressure $P(x, z, t)$, as shown in Figure 2, that is a scalar field. These Eulerian dynamic and kinematic fields for the irrotational flow of an inviscid, incompressible fluid computed from a scalar velocity potential $\Phi(x, z, t)$.

The dynamic component $p(x, z, t)$ of the total pressure field $P(x, z, t)$ computed from a scalar velocity potential by the unsteady Bernoulli equation according to

$$\frac{P(x, z, t)}{\rho} = \frac{p(x, z, t)}{\rho} + \frac{p_s(x, z, t)}{\rho} = \left(\frac{\partial \Phi(x, z, t)}{\partial t} - \frac{|\nabla \Phi(x, z, t)|^2}{2} \right) - gz \quad (1.2)$$

where ρ is the mass density of fluid, $gz = p_s(z) / \rho$ is the hydrostatic pressure, $|\vec{\nabla}\Phi(x, z, t)|^2$ is the fluid velocity squared $\vec{q} \bullet \vec{q} = |\vec{q}|^2$, and the Bernoulli constant $Q(t)$ has been absorbed into $\Phi(x, z, t)$.

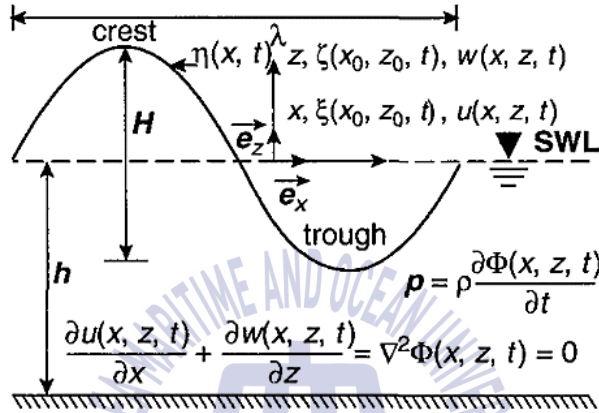


Figure 2 Definition sketch for dimensional linear wave theory (LWT) boundary value [19]

The linear wave theory can be applied with excellent accuracy in estimating the kinematic properties of waves when a ratio of wave height to wavelength H/λ is 1/50 or less. The brief nomenclature of a linear water wave are illustrated in Figure 3, and the mathematical expressions for the wave period and free-surface displacement are described respectively as

$$T = 2\pi \left[\frac{2\pi g}{\lambda} \tanh\left(\frac{2\pi h}{\lambda}\right) \right]^{-1/2} = \frac{1}{f} = \frac{2\pi}{\omega} \quad (1.3)$$

$$\eta = \frac{H}{2} \cos\left(\frac{2\pi x}{\lambda} - \frac{2\pi t}{T}\right) \quad (1.4)$$

where f is the wave frequency, ω is the circular wave frequency ($2\pi f$), and h is the water depth from the bottom. The wave period T is commonly considered to be invariant with both depth h and time t , however, it can be changed over long travel distances. Individual waves travel at a phase velocity c , illustrated by equation (1.5) as

$$c = \frac{\lambda}{T} = \frac{gT}{2\pi} \tanh(kh) \quad (1.5)$$

where k is the wave number defined by

$$k = \frac{2\pi}{\lambda} \quad (1.6)$$

The horizontal and vertical velocity components of water particles within the traveling waves are described respectively as below

$$u = \frac{\pi H}{T} \times \frac{\cosh[k(z+h)]}{\sinh(kh)} \times \cos(kx - \omega t) \quad (1.7)$$

and

$$w = \frac{\pi H}{T} \times \frac{\sinh[k(z+h)]}{\sinh(kh)} \times \sin(kx - \omega t) \quad (1.8)$$

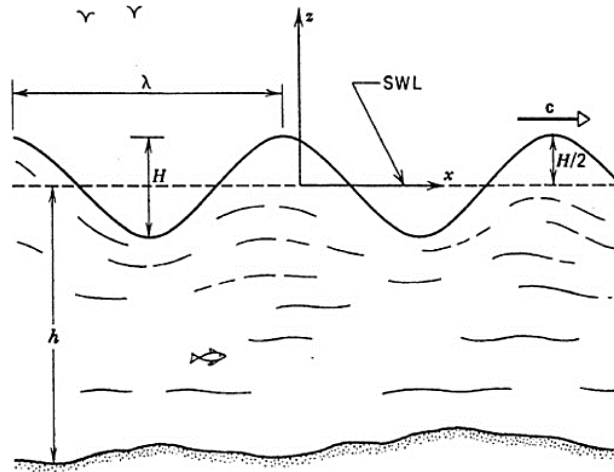


Figure 3 Nomenclature of a linear water wave, having a sinusoidal profile [20]

It is noted that the previous equations for linear wave theory are significantly varied depending on properties of wave under various water depth conditions, and the summary of linear wave characteristics at different wave conditions are represented in Table 3. As shown in Figure 4, the wave depth is demonstrated by the ratio of the wavelength to the water depth. When the wave depth is deeper than one-half of its wavelengths, the deep-water waves occur, usually driven by wind. Under this condition, the water particles travel in circular paths with diameters that reduce exponentially with water depth as described in Figure 4 (a). The intermediate or transitional waves in Figure 4 (b) commonly occur in water, where $1/2 < h/\lambda < 1/20$. The paths of the intermediate water particles tend to be elliptical with major and minor axes that reduce with the water depth due to bottom friction. Referring to Figure 4 (c), the shallow-water waves appear where its depth is less than $1/20$ of the wavelength. The water particles move in elliptical paths and interface with the ocean floor that make the speed of waves slower [20].

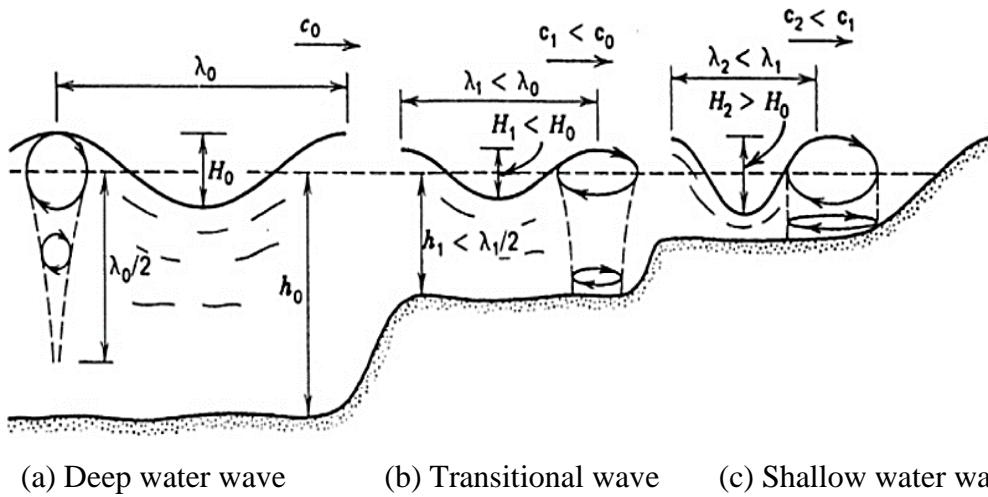


Figure 4 Properties of waves under several depth conditions: (a) deep water, (b) intermediate water, (c) shallow water [20]



Table 3 Summary of linear (Airy) wave theory characteristics [21]

Wave properties	Deep wave ($d / \lambda > 1/2$)	Transitional wave ($1/20 < d / \lambda < 1/2$)	Shallow wave ($d / \lambda < 1/20$)
Wave profile	$\eta = \frac{H}{2} \cos\left(\frac{2\pi x}{\lambda} - \frac{2\pi t}{T}\right)$	$\eta = \frac{H}{2} \cos\left(\frac{2\pi x}{\lambda} - \frac{2\pi t}{T}\right)$	$\eta = \frac{H}{2} \cos\left(\frac{2\pi x}{\lambda} - \frac{2\pi t}{T}\right)$
Wave celerity	$c = \frac{gT}{2\pi}$	$c = \frac{gT}{2\pi} \tanh\left(\frac{2\pi d}{\lambda}\right)$	$c = \sqrt{gd}$
Wavelength	$\lambda = \frac{gT^2}{2\pi}$	$\lambda = \frac{gT^2}{2\pi} \times \tanh\left(\frac{2\pi d}{\lambda}\right)$	$\lambda = T\sqrt{gd}$
Water particle velocity			
(a) Horizontal	$u = \frac{\pi H}{T} e^{\left(\frac{2\pi z}{\lambda}\right)} \cos \theta$	$u = \frac{H}{2} \frac{gT}{\lambda} \frac{\cosh[2\pi(z+d)/\lambda]}{\cosh(2\pi d/\lambda)} \cos \theta$	$u = \frac{H}{2} \sqrt{\frac{g}{d}} \cos \theta$
(b) Vertical	$w = \frac{\pi H}{T} e^{\left(\frac{2\pi z}{\lambda}\right)} \sin \theta$	$w = \frac{H}{2} \frac{gT}{\lambda} \frac{\sinh[2\pi(z+d)/\lambda]}{\cosh(2\pi d/\lambda)} \sin \theta$	$w = \frac{H\pi}{T} \left(1 + \frac{z}{d}\right) \sin \theta$
Water particle displacements			
(a) Horizontal	$\xi = -\frac{H}{2} e^{\left(\frac{2\pi z}{\lambda}\right)} \sin \theta$	$\xi = -\frac{H}{2} \frac{\cosh[2\pi(z+d)/\lambda]}{\sinh(2\pi d/\lambda)} \sin \theta$	$\xi = -\frac{HT}{4\pi} \sqrt{\frac{g}{d}} \sin \theta$
(b) Vertical	$\xi = \frac{H}{2} e^{\left(\frac{2\pi z}{\lambda}\right)} \cos \theta$	$\xi = \frac{H}{2} \frac{\sinh[2\pi(z+d)/\lambda]}{\sinh(2\pi d/\lambda)} \cos \theta$	$\xi = \frac{H}{2} \left(1 + \frac{z}{d}\right) \cos \theta$
Subsurface pressure	$p = \rho g \eta \times e^{\left(\frac{2\pi z}{\lambda}\right)} - \rho g z$	$p = \rho g \eta \frac{\cosh[2\pi(z+d)/\lambda]}{\cosh(2\pi d/\lambda)} - \rho g z$	$p = \rho g(\eta - z)$

1.4 Objective of research

The aim of this research is to investigate the cross-flow air turbine for OWC wave energy converter. The cross-flow air turbine have not been applied as an air turbine for OWC wave energy converter since it has a potential competitiveness of air turbine for OWCs compared to other types of air turbines.

First, the performance analysis for the cross-flow air turbine have been processed to obtain the performance of the turbine in various range of the flow rate with different rotational speed of the blade. After then, the orifice plate as substitute for turbine damping effects have numerically studied by CFD. In addition, the comparative study between CFD analysis and experiment was proposed for verification of CFD result.



Chapter 2. CFD analysis of a cross-flow air turbine

2.1 ANSYS CFD Code

2.1.1 DISCRETIZATION OF THE GOVERNING EQUATIONS

ANSYS CFX employs an element-based finite volume method, which first involves discretizing the spatial domain using a mesh [22]. The mesh is applied to build finite volumes, which are utilized to conserve relevant quantities of mass, momentum and energy. A typical configuration of two-dimensional mesh in Figure 5 is illustrated (actual mesh is three-dimensional shape). All fluid properties and solution variables are stored at the nodes, called mesh vertices. The control volume (the shaded area) is built around each mesh node by the median dual, defined by lines connected the centers of the edges and element centers surrounding the node.

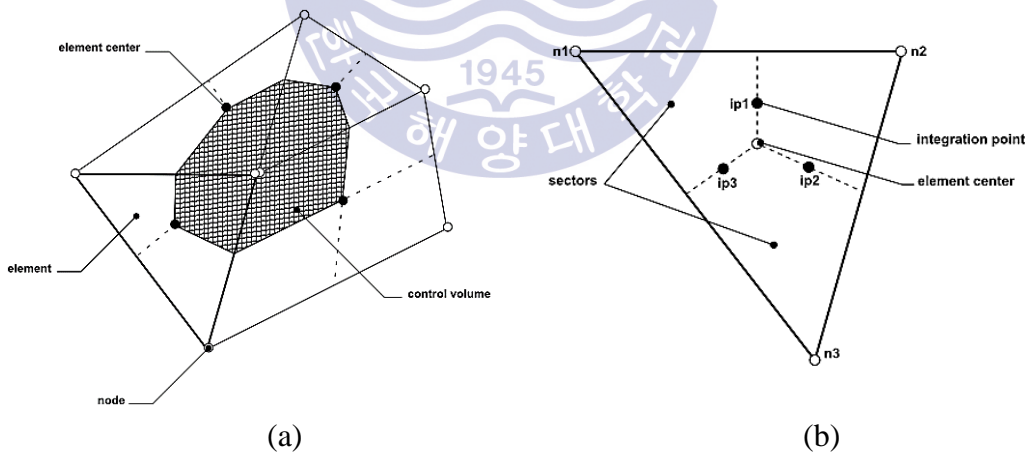


Figure 5 Configuration of control volume definition (a) and mesh element (b) [22]

It is considered that the conservation equations for mass, momentum and a passive scalar are expressed in Cartesian coordinates for understanding of the finite volume

methodology as shown in Equation (2.1), (2.2), (2.3) respectively, which the first-order backward Euler scheme has been assumed in.

$$\frac{\partial \rho}{\partial t} + \frac{\partial}{\partial x_j}(\rho U_j) = 0 \quad (2.1)$$

$$\frac{\partial}{\partial t}(\rho U_i) + \frac{\partial}{\partial x_j}(\rho U_j U_i) = -\frac{\partial P}{\partial x_i} + \frac{\partial}{\partial x_j} \left(\mu_{eff} \left(\frac{\partial U_i}{\partial x_j} + \frac{\partial U_j}{\partial x_i} \right) \right) \quad (2.2)$$

$$\frac{\partial}{\partial t}(\rho \varphi) + \frac{\partial}{\partial x_j}(\rho U_j \varphi) = \frac{\partial}{\partial x_j} \left(\Gamma_{eff} \left(\frac{\partial \varphi}{\partial x_j} \right) \right) + S_\varphi \quad (2.3)$$

The previous governing equations are integrated over each control volume, and the volume integrals involving divergence and gradient operators are converted to surface integrals by applying Gauss' Divergence Theorem as follows

$$\frac{d}{dt} \int_V \rho dV + \int_S \rho U_j dn_j = 0 \quad (2.4)$$

$$\frac{d}{dt} \int_V \rho U_i dV + \int_S \rho U_j U_i dn_j = - \int_S \rho dn_j + \int_S \mu_{eff} \left(\frac{\partial U_i}{\partial x_j} + \frac{\partial U_j}{\partial x_i} \right) dn_j + \int_V S_{U_i} dV \quad (2.5)$$

$$\frac{d}{dt} \int_V \mu \varphi dV + \int_S \mu U_j \varphi dn_j = \int_S \Gamma_{eff} \left(\frac{\partial \varphi}{\partial x_j} \right) dn_j + \int_V S_\varphi dV \quad (2.6)$$

where S and V denote surface and volume regions of integration respectively, and dn_j is the differential Cartesian components of the outward normal surface vector. The surface integrals indicate the summation of the fluxes, and the volume integrals illustrate accumulation or source terms.

Volume integrals are discretized within each element sector that is accumulated to the control volume to which the sector belongs. In addition, the discretized surface integrals at the integration points (ipn) located at the center of each surface segment within an element distribute to the adjacent control volumes. It is guaranteed the surface integrals to be locally conservative since the surface integrals are equal and opposite for control volumes adjacent to the integration points. After discretizing both the surface and volume integrals, the integral equations become as follows:

$$V \left(\frac{\rho - \rho^0}{\Delta t} \right) + \sum_{ip} \dot{m}_{ip} = 0 \quad (2.7)$$

$$V \left(\frac{\rho U_i - \rho^0 U_i^0}{\Delta t} \right) + \sum_{ip} \dot{m}_{ip} (U_i)_{ip} = \sum_{ip} (P \Delta n_i)_{ip} + \sum_{ip} \left(\mu_{eff} \left(\frac{\rho U_i}{\rho x_j} + \frac{\rho U_j}{\rho x_i} \right) \Delta n_j \right)_{ip} + \bar{S}_{U_i} V \quad (2.8)$$

$$V \left(\frac{\rho \varphi - \rho^0 \varphi^0}{\Delta t} \right) + \sum_{ip} \dot{m}_{ip} \varphi_{ip} = \sum_{ip} \left(\Gamma_{eff} \left(\frac{\partial \varphi}{\partial x_j} \right) \Delta n_j \right)_{ip} + \bar{S}_{\varphi} V \quad (2.9)$$

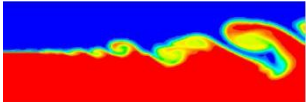
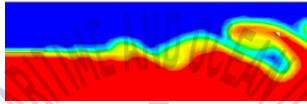
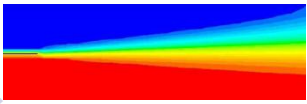
where V and $\dot{m}_{ip} = (\rho U_j \Delta n_j)_{ip}$ is the control volume, Δt is the time step, Δn_j is the discrete outward surface vector, the subscript ip represents evaluation at an integration point, and the superscript 0 denotes the old time level.

2.1.2 TURBULENCE MODEL

One of the significant problems in fluid engineering field is the accurate prediction of flow separation at near area from a surface or edge. A random and chaotic state of flow behavior develops in which the pressure and velocity vary continuously with time within substantial regions of flow [23]. The flow behavior in complex turbulent

regime can be tackled numerically through CFD techniques such as the finite volume methods, and there are several computational approaches for the turbulent flow structures. A brief overview of main three computational approaches is illustrated in Table 4 [22].

Table 4 Overview of turbulent flow simulation methods [22]

DNS (Direct Numerical Simulation)	SRS (Scale Resolving Simulations)	RANS (Reynolds Averaged Navier-Stokes Simulation)
		
<ul style="list-style-type: none"> - All turbulent flows can be simulated numerically by solving the full unsteady Navier-Stokes equations - Resolving the whole spectrum of scales, and no modelling is required - Not practical for industry fields since prohibitive resources are required 	<ul style="list-style-type: none"> - Solving the spatially averaged Navier-Stokes equations - The motion of large eddies are directly resolved, but eddies smaller than the mesh are modelled - Including Large Eddy Simulation (LES) method - Less expensive than DNS, the relative huge amount of computational resources are required 	<ul style="list-style-type: none"> - The most widely applied approach for industry fields - Solving time-averaged Navier-Stokes equations Modelling turbulent flow and steady state solutions are possible, but larger eddies are not resolved

As mentioned previously, the method of DNS and SRS is not suitable for most industry fields due to its prohibitive resources. Therefore, the RANS (Reynolds Averaged Navier-Stokes Simulations) is typically applied in CFD tools due to its capacity of solving problems effectively. In the RANS method, two-equation

turbulence models are the most widely used, as they provide a great compromise between numerical effort and computational accuracy. The $k - \omega$ based SST (Shear Stress Transport) model have been applied to effectively blend the robust and accurate formulation of the $k - \omega$ model in the near-wall area with the free-stream independence of the $k - \varepsilon$ model in the far region. The BSL (Baseline) model blends the advantages of the $k - \varepsilon$ and Wilcox model. However, it has still deficiency of predicting onset and amount of flow separation from smooth surfaces properly since both models do not consider the transport of the turbulent shear stress, that induce an overprediction of the eddy-viscosity. A limiter to the eddy-viscosity formulation can offers the proper behavior of transport as follows,

$$v_t = \frac{a_1 k}{\max(a_1 \omega, S F_2)} \quad (2.10)$$

where $v_t = \mu_t / \rho$, F_2 is a blending function similar to F_1 , which restricts the limiter to the wall boundary layer, S is the strain rate.

The blending functions are crucial to achieve the success of the method. Its formulations are based on the flow variables and the distance to the nearest surface.

$$F_1 = \tanh(\arg_1^4) \quad (2.11)$$

with

$$\arg_1 = \min \left(\max \left(\frac{\sqrt{k}}{\beta' \omega y}, \frac{500\nu}{y^2 \omega} \right), \frac{4\rho k}{CD_{k\omega} \sigma_{\omega 2} y^2} \right) \quad (2.12)$$

where y is the distance to the nearest wall, ν is the kinematic viscosity and

$$CD_{k\omega} = \max \left(2\rho \frac{1}{\sigma_{\omega 2} \omega} \times \frac{\partial k}{\partial x_j} \times \frac{\partial \omega}{\partial x_j}, 1.0 \times 10^{-10} \right) \quad (2.13)$$

$$F_2 = \tanh(\arg_2^2) \quad (2.14)$$

$$\arg_2 = \max \left(\frac{\sqrt{k}}{\beta^1 \omega y}, \frac{500\nu}{y^2 \omega} \right) \quad (2.15)$$

The SST or BSL model require a node distance to the nearest wall for the performance of the blending between $k - \varepsilon$ and $k - \omega$ methods. The generalized form of the wall scale equation can be represented with a uniform source term of unity as follows,

$$\nabla^2 \phi = -1 \quad (2.16)$$

$$\text{Wall distance} = -|\nabla \phi| + \sqrt{|\nabla \phi|^2 + 2\phi} \quad (2.17)$$

where ϕ is the wall scale, always positive since the wall distance is always positive.

2.2 Design of cross-flow turbine

A direct method to calculate the general dimension and flow parameters for the runner and nozzle section was utilized referring to Mockmore et al. [16] and Fukutomi et al. [17] respectively. The designed cross-flow air turbine is illustrated in Figure 6 and the design parameters are described in Table 5. The cross-flow turbine in its simplest form consists of a nozzle and a runner section. The induced air flow due to increasing wave level moves through the rectangular cross-section nozzle and flows into the runner. When the wave level is decreased, the air flow from

the atmosphere passes through the symmetric shape of nozzle and enters the runner again. Thus, the circulating air flow is continuously moving through the nozzles and runner section that rotate the blade in uni-direction.

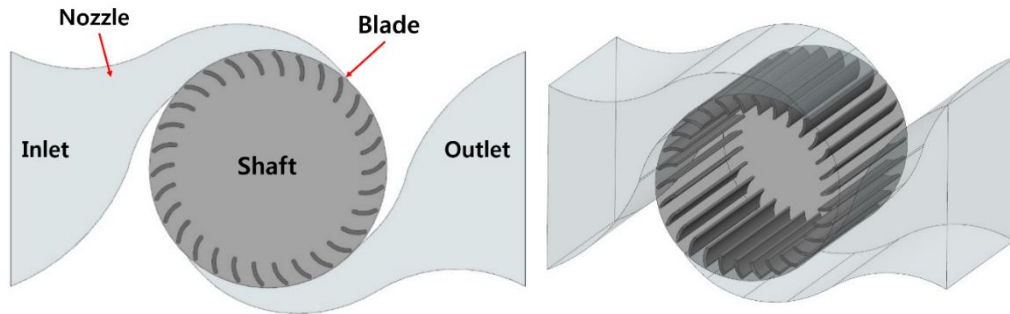


Figure 6 Configuration of cross-flow air turbine

Table 5 Design parameters for the cross-flow air turbine

Design Parameters	Value
Outer Diameter	1.5m
Inner Diameter	1.2m
No. Blade	30
Nozzle Entry Angle (δ)	90°
Angle of Attack (α)	18°
Blade Inlet Angle(β_1)	30°
Blade Exit Angle(β_2)	90°
Rotational Speed (N)	16, 32, 48, 64 rpm
Nozzle tip angle (α')	15°
Nozzle throat width ($S_0/R_1 \delta$)	0.26

2.3 Steady State simulation

In this section, the performance study of the designed cross-flow air turbine for OWC wave energy converter as the beginning stage of this research will be discussed. For its simplicity of investigating the turbine performance, several assumptions were applied: incompressible air and linear wave and air flow. In addition, the study of

single turbine section excluding the OWC chamber with wave motion was processed for efficient analysis.

2.3.1 NUMERICAL ANALYSIS SETUP

CFD simulations of the cross-flow turbine in 3D steady state were processed using the commercial CFD code ANSYS CFX 14.0. The single domain of the cross-flow air turbine excluding OWC chamber and wave elevation was determined for simplicity of analysis. The entire domain of the turbine is designed as 1/10 of symmetric domain for efficient simulation as shown in Figure 8, and also it was checked that there is no significant difference between full and 1/10 of symmetric model. For CFD simulation, the mesh comprising fine hexahedral grids with 1.76×10^6 nodes was generated, shown in Figure 7, by ANSYS ICEM CFD so that the high accuracy of analysis results are obtained. The steady state type simulation were processed with SST turbulence model. The boundary condition for the simulation was set with different rotational speed of 16, 32, 48, 64 rpm and uni-directional inlet air velocity from 2m/s to 40 m/s, calculated using the design wave elevation and periods, for full scale conditions. The single air phase in boundary condition was used which allows only air to move through the turbine. General Grid Interface (GGI) method was applied for the mesh connection between each parts with the interface. Overall boundary conditions for simulation is depicted in Table 6.

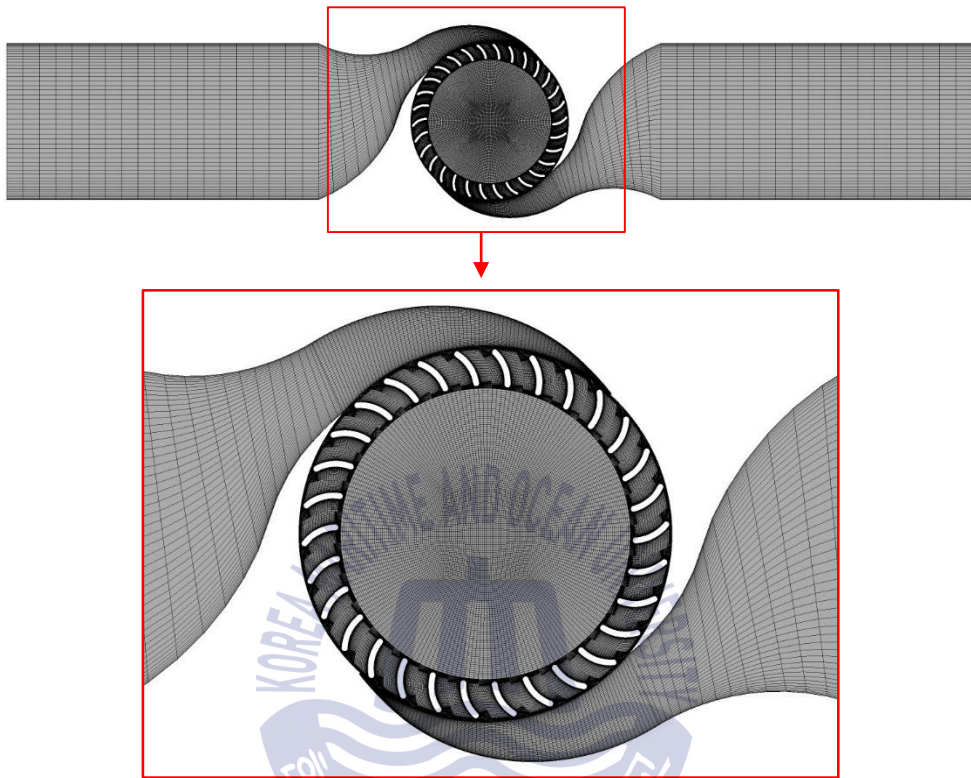


Figure 7 Meshing of the cross-flow air turbine by ICEM CFD

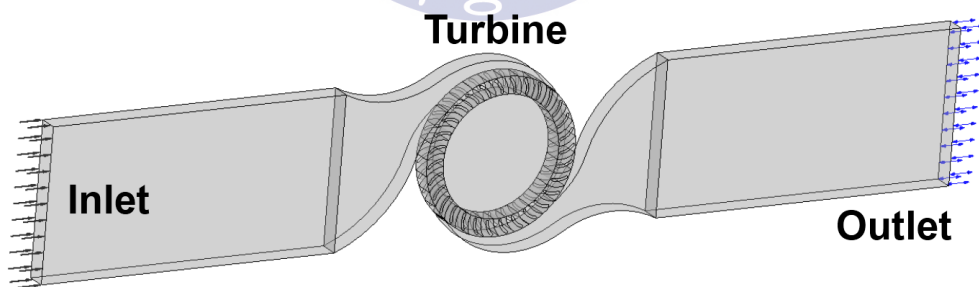


Figure 8 Configuration of CFX pre setup domain for the cross-flow air turbine in steady state

Table 6 Boundary condition of CFX pre setup for the cross-flow air turbine in steady state simulation

Numerical Methods	Mesh type	Hexahedral
	No. Mesh node	1.76×10^6
	Simulation type	Steady state
	Turbulence model	Shear Stress Transport (SST)
	Fluid phase	1 phase (air)
	Physical timescale	$1/\omega$
Boundary Conditions	Inlet	Mass flow rate
	Outlet	Opening
	Rotational Speed	16, 32, 48, 64 rpm (Full scale)
	Wall	No-slip
	Rotor Stator Interface	Frozen Rotor
	Model Scale	1/10 (Symmetry in width)
	y+	<0.219

2.3.2 CFD RESULT AND DISCUSSION

The cross-flow air turbine have its division of runner flow passage as shown in Figure 9. The main characteristic of the turbine is that the rectangular cross-sectional air jet from the nozzle passes twice the rotor blades. Air flow moves through the rectangular cross-section of the nozzle, enters and rotates the runner of stage 1. Air leaving through curve edge of the runner then passes into the runner of stage 2. The energy conversion from kinematic energy of the air flow to mechanical energy occurs twice; first huge impingement of air on the blade upon entry, and then the air strikes the blades upon exit from the runner.

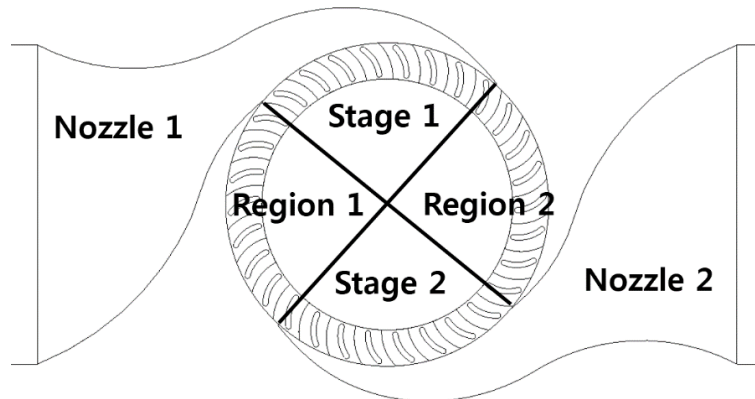


Figure 9 Schematic configuration of the cross-flow air turbine with division of runner flow passage

Figure 10 presents the velocity vectors in the internal air flow field of the turbine domain. The behavior of the air flow from inlet tends to be accelerated just before the runner blade inlet due to narrow cross-sectional area of the nozzle. The air flow just leaving the stage 1 have reduced velocity due to the energy conversion from kinematic energy of air flow to mechanical energy of the rotor. The air velocity becomes accelerated until just before the runner inlet of the stage 2, and again the energy conversion of air flow takes place passing through the runner of the stage 2. However, a large recirculation flow is captured in the central region of the rotor that possibly induces the loss of energy conversion.

Static pressure contours in the internal airflow field of the turbine domain is illustrated in Figure 11. The fluid pressure from the nozzle inlet decreased until just before the stage 1 which increases the fluid velocity, and it increases the fluid power. The pressure drop represents the energy conversion, and the larger amount of energy transfer during passing through the stage 1 than the stage 2 was observed. In addition,

the low level of pressure distribution at the central region represents the large recirculation flow region.

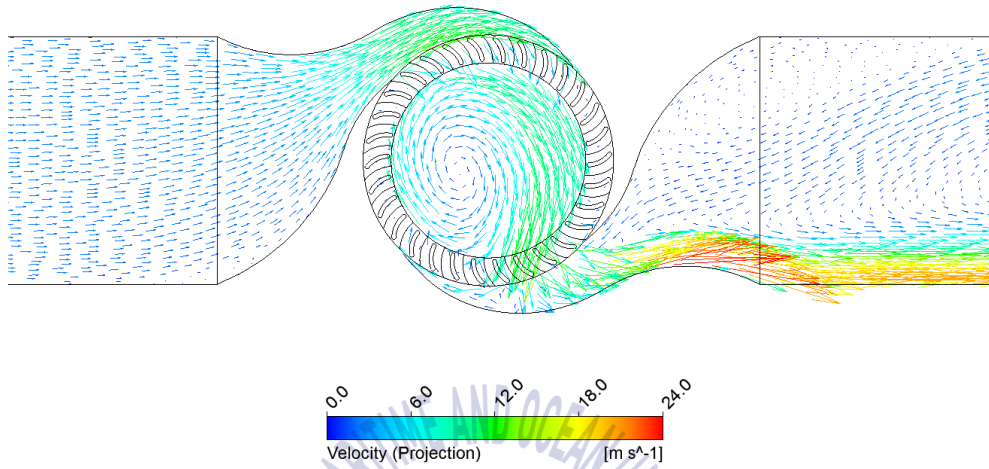


Figure 10 Velocity vectors in the flow field of the turbine domain at 32rpm rotational speed and 7m/s inlet velocity

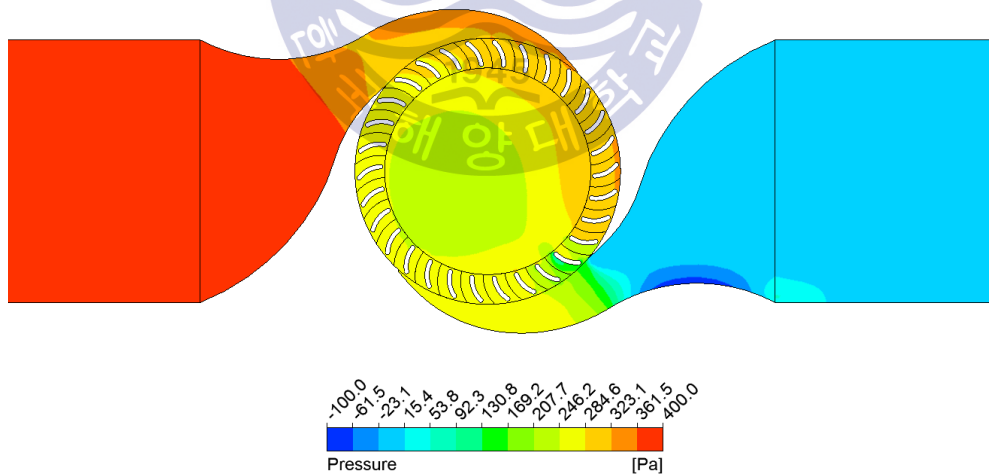


Figure 11 Pressure contours in the flow field of the turbine domain at 32rpm rotational speed and 7m/s inlet velocity

It is vital to be able not only to make use of model testing but also to relate the results of the small scale model measurements to the expected performance of general larger or full scale model. With the aid of dimensional analysis, this issue can be settled. In addition, the analysis method requires several assumptions; incompressible flow that is the fluid density is uniform and constant [24].

The performance of an equipment is determined by a set of main five variables as follows; its size (possibly its outer diameter of rotor D), two fluid variables (the density ρ and the viscosity μ), and two control variables (the rotational speed Ω and the flow rate Q). With the variables, the several dimensionless coefficients can be developed, and these similarity laws allow the result of model testing to be related to the performance of a geometrically similar equipment of different size, rotational speed, with different density of a fluid. In addition, the effect of varying Reynolds number is commonly adopted into account as a correction based on more or less empirical laws. Main four dimensionless coefficients applied for the analysis of the cross-flow air turbine are depicted as follows,

Torque coefficient

$$\Pi = \frac{T}{\rho \times \Omega^2 \times D^5} \quad (2.18)$$

where T is the torque of the turbine.

Flow coefficient

$$\Phi = \frac{Q}{\Omega \times D^3} \quad (2.19)$$

Pressure coefficient

$$\psi = \frac{p}{\rho \times \Omega^2 \times D^2} \quad (2.20)$$

where p is the pressure head available to the turbine (normally difference between stagnation pressure at inlet and outlet of the turbine).

Aerodynamic efficiency

$$\eta = \frac{\Pi}{\psi \times \Phi} \quad (2.21)$$

With the dimensional analysis method, the non-dimensional performance of the cross-flow air turbine can be obtained as shown in Figure 12. The turbine was investigated by varying the rotational speed of blades (16, 32, 48 and 64 rpm for full scale) and the inlet air velocity (from 2m/s to 40m/s). The peak performance of the turbine was 0.587 at the rotational speed of 48 rpm and the inlet velocity of 12m/s. All performance for different rotational speed of the turbine have relatively same tendency although the performance for 16 rpm rotational speed have slightly less performance than the others. After the stall region, the performance curves tend to significantly drop, and it means that the design flow rate for the turbine performance would be in low range. It is noted that the investigation of this turbine is the early stage of research, thus it needs to be improved by further modification of geometries or possible variables.

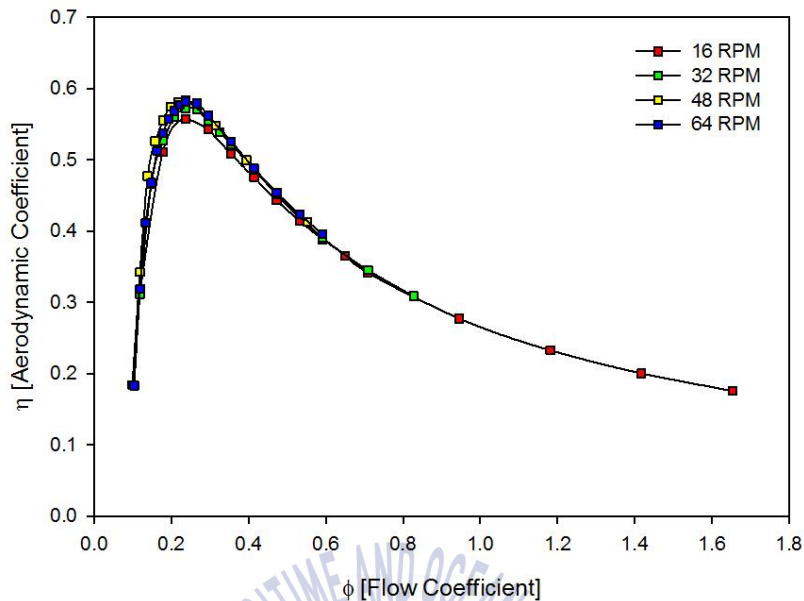


Figure 12 Performance of the cross-flow air turbine by dimensionless analysis

2.4 Transient simulation

The aim of this section is to investigate the behavior of the model-scaled cross-flow turbine in bi-directional flow conditions by CFD. The bi-directional flow conditions were determined based on the real sea conditions of 2m significant wave height and 5, 6, 7 and 8 sec wave periods. The 1/16 of model scale was adopted since the performance of the model-scaled turbine will be compared to the validation of the orifice plates as the cross-flow air turbine substitute by CFD and experiment. The corresponding model-scaled significant wave height and periods are 0.125m and 1.25-2.0 sec respectively. The simulation of the turbine excluded the wave motion in OWC chamber, and the piston motion of air flow at the inlet of the nozzle was substituted for its efficient calculation with linear wave theory.

2.4.1 NUMERICAL SETUP

The entire domain of the 1/16 scaled turbine model excluding OWC chamber and wave motion is depicted as shown in Figure 13. The mesh comprising fine hexahedral grids with 2.49×10^6 nodes, same meshing formation as previous turbine domain, was generated. The transient type of simulation was adopted so that the bi-directional flow condition can be set on the turbine. The bi-directional flow having sinusoidal pattern, calculated using the linear wave theory with 0.125m wave height and 0.125-2 sec periods, allows the volume of air induced due to wave motion to pass through the turbine. The sinusoidal air velocity was adopted for the inlet condition. The rotational speed of the blade was determined as 1000rpm, 1/16 scaled of 16rpm prototype speed. The overall boundary conditions for the simulation is illustrated in Table 7.

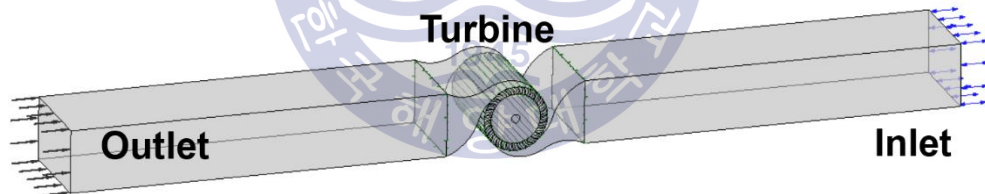


Figure 13 Configuration of CFX pre setup domain for the cross-flow air turbine in transient simulation

Table 7 Boundary condition of CFX pre setup for the cross-flow air turbine in transient simulation

Numerical Methods	Mesh type	Hexahedral
	No. Mesh node	2.49×10^6
	Simulation type	Transient
	Turbulence model	Shear Stress Transport (SST)
	Fluid phase	1 phase (air)
Boundary Conditions	Inlet	Sinusoidal air velocity
	Outlet	Opening
	Period	1.25, 1.5, 1.75 and 2.0 sec
	Wave height	0.125m
	Rotational Speed	1000 rpm
	Wall	No-slip
	Rotor Stator Interface	Frozen Rotor
	Model Scale	1/16

2.4.2 DATA ANALYSIS

In this section, the process of phase averaging will be described. The purpose of the phase averaging is not only to obtain smooth graph from unstable data from simulation and experiment but also to represent all data, which have different time steps, in one single phase so that all data can be compared in same time range.

Time-series data is cyclical and it is represented into one phase single time-series by a phase averaging method. The time of the time-series data is converted to non-dimensionalized by substituting the actual time with a non-dimensional phase (t/T) which is depicted in Figure 14. First, the time series is divided into segments of repeating cycles with zero-up-crossing. Then, the phase of the data points is allocated by subtracting the previous adjacent zero-up-crossing time and dividing by the cycle period [25] as shown in Equation (2.22), where time of zero crossing of immediate

cycle (T_{zero}), time of zero-crossing of end of immediate cycle (T_{zero+1}), measured time ($T_{measured}$) and $0 \leq t/T < 1$.

$$\frac{t}{T} = \frac{T_{measured} - T_{zero}}{T_{zero+1} - T_{zero}} \quad (2.22)$$

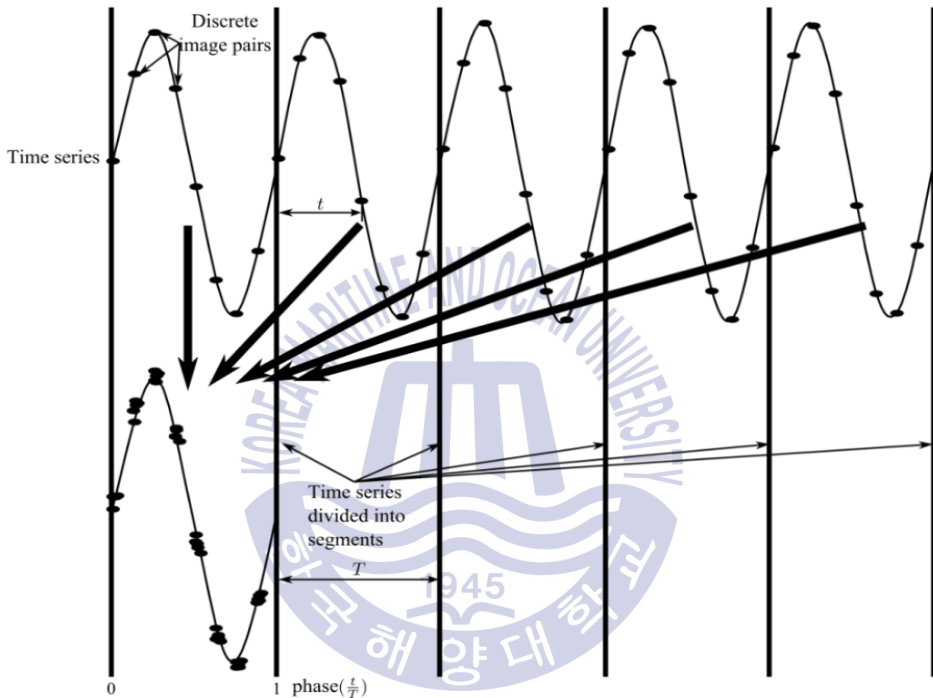


Figure 14 Visual configuration of the division of time series data into segments for phase averaging [25]

Figure 15 illustrate one of examples of phase-sorted data for the pressure gap between upstream and downstream of chamber and the flow rate through the turbine. The width of the phase range is depicted in $0 \leq t/T < 1$, where $t=0.005$, and equal sized non-overlapping windows is in the width. The number of cycles varies between 4 to 6 cycles according to each period being simulated or tested. The time-series

cycles of the pressure gap have more irregular patterns compared to the cycles of flow rate because the air pressure is changed drastically due to its compressibility.

The irregular phase-sorted data becomes smoother by an ensemble averaging, and one of examples of ensemble-averaged profiles is illustrated in Figure 16. The irregular data points of all cycle in every 0.01 phase are phase-averaged to one single data point, totally 50 data points in one phase.

From the ensemble-averaged graph, it can be seen that the pressure drop between upstream and downstream of the turbine has a zero at a phase value of 0.25, whereas the graph of the flow rate reaches the peak. The movement of the wave elevation have a same behavior of a piston in engine. When the wave elevation is positioned at the center of the chamber, the wave velocity has a maximum speed due to acceleration. However, unlike the engine piston, the maximum chamber pressure is not observed when the wave is at the end of stroke since the air chamber is opened to atmosphere. Thus, the maximum pressure is obtained with the maximum flow rates.

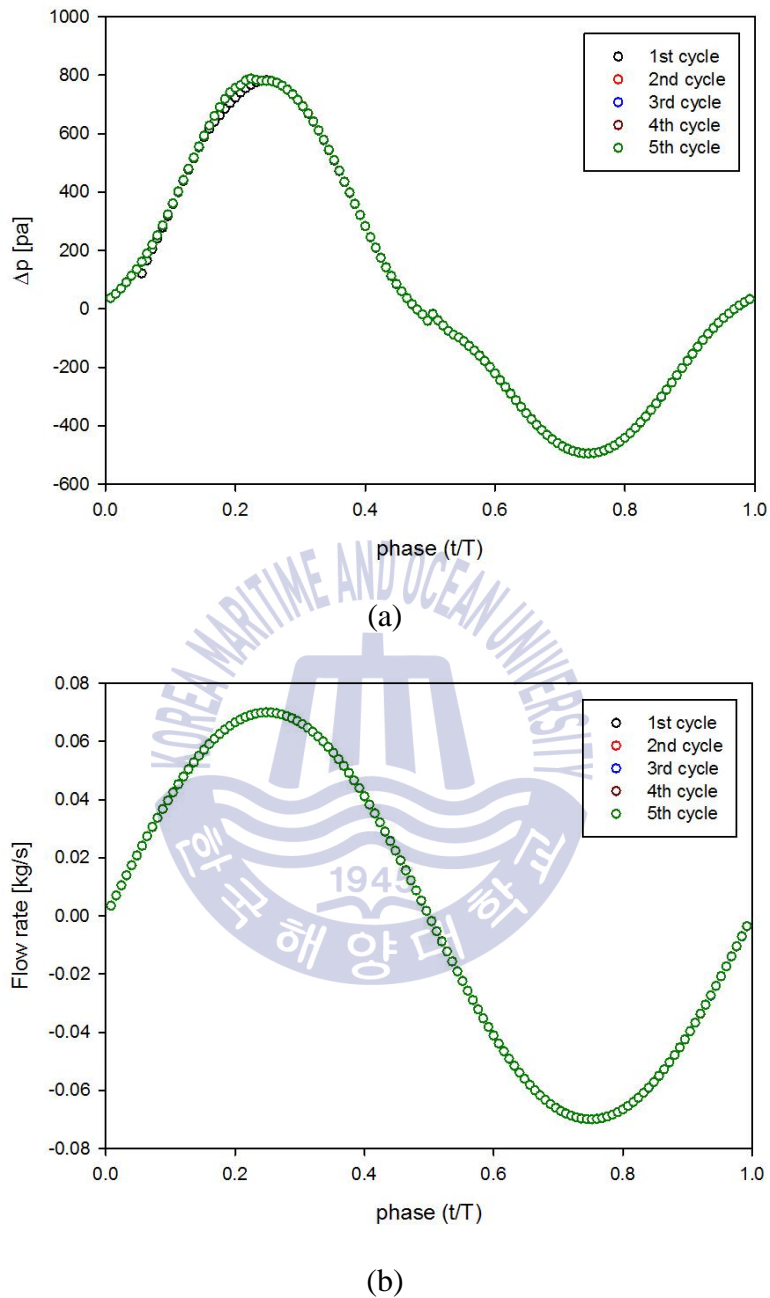
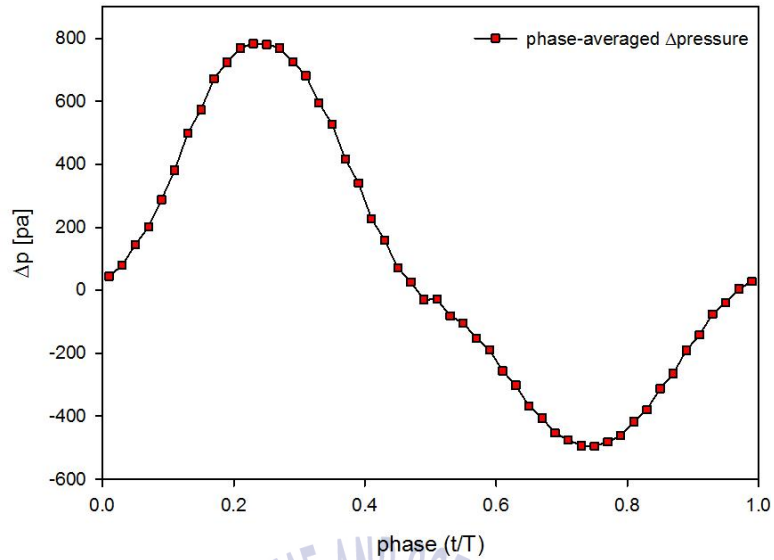
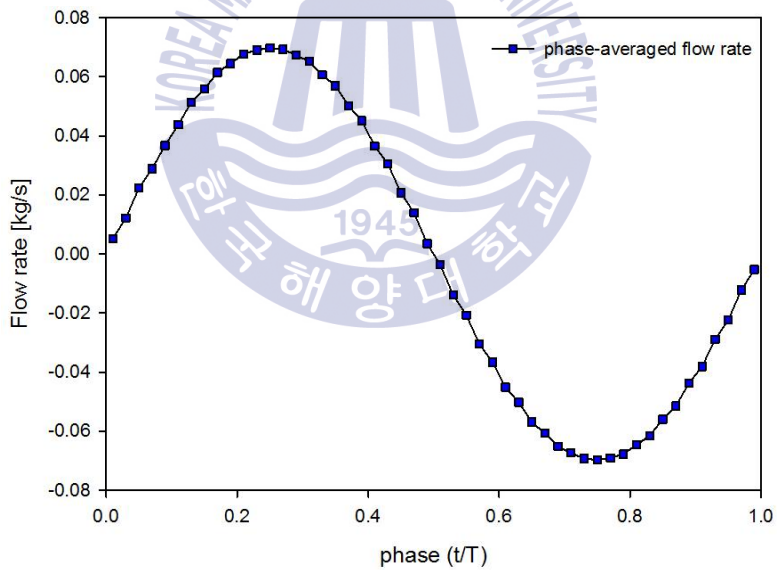


Figure 15 Representation of times series cycles for (a) pressure gap between upstream and downstream and (b) flow rate through the turbine in one segment by phase averaging (T=1.5sec)



(a)

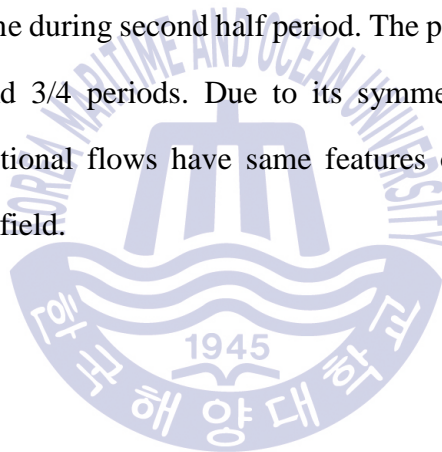


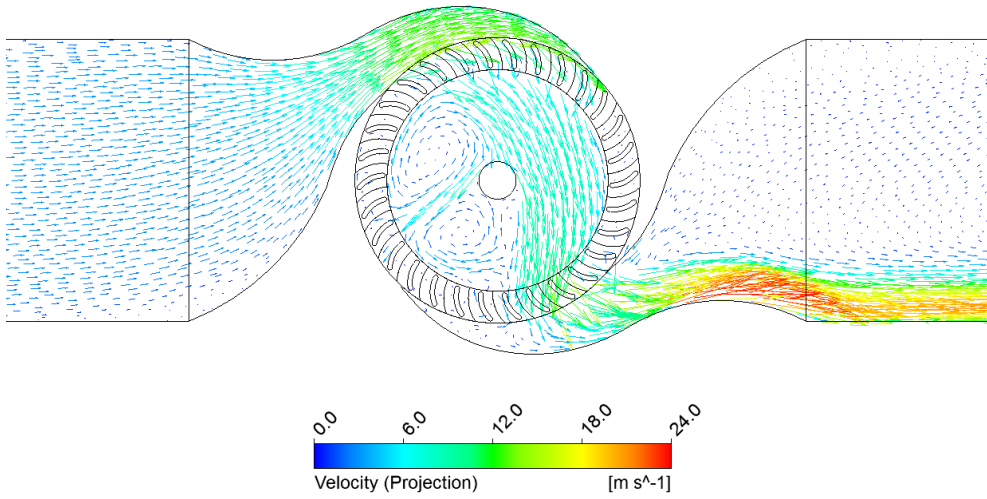
(b)

Figure 16 Phase-averaged profile of (a) pressure gap and (b) flow rate ($T=1.25\text{sec}$)

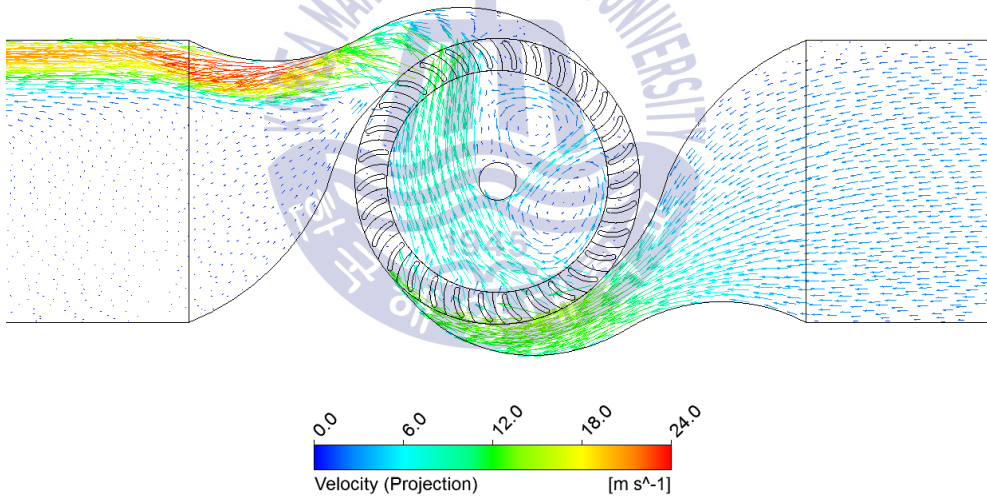
2.4.3 CFD RESULT AND DISCUSSION

CFD simulation under the condition of bi-directional flow for the performance of the model scaled cross-flow air turbine has been processed. The behavior of internal flow field of the turbine is represented with the velocity vector and the static pressure contours as shown in Figure 17 and Figure 18 respectively, and it has relatively same flow behavior as the previous steady state simulation. The bi-directional air flow passes through the turbine; first incoming air flow from the nozzle 1 moves through the turbine during first half period, and opposite directional flow from the nozzle 2 passes through the turbine during second half period. The peak velocity and pressure are indicated at 1/4 and 3/4 periods. Due to its symmetric geometry, the flow behavior for both directional flows have same features of velocity and pressure distribution on the flow field.



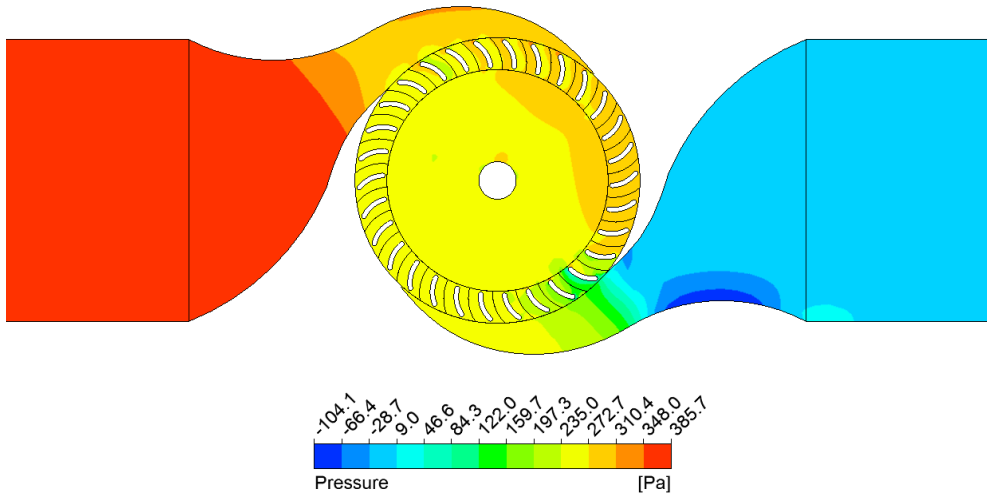


(a) 1/4 period of one cycle

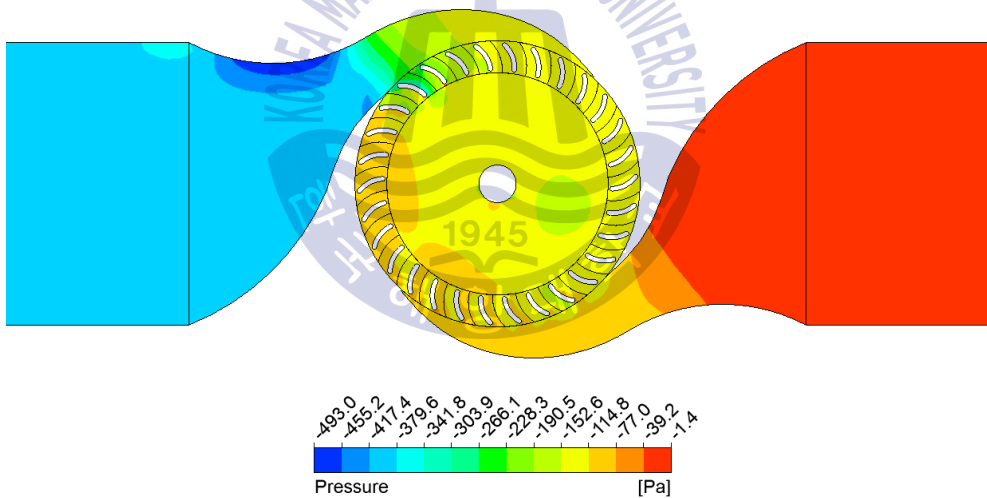


(b) 3/4 period of one cycle

Figure 17 Velocity vectors in the flow field of the turbine domain at 1000rpm rotational speed and 2 sec period



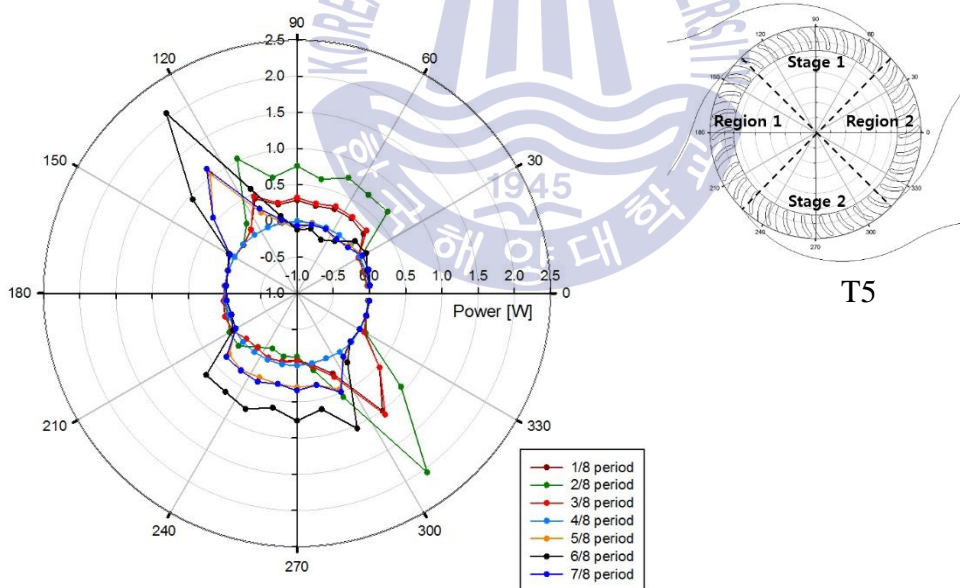
(a) 1/4 period of one cycle



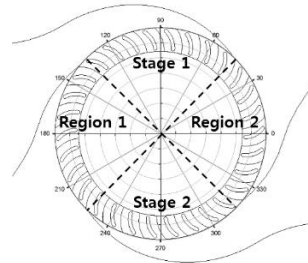
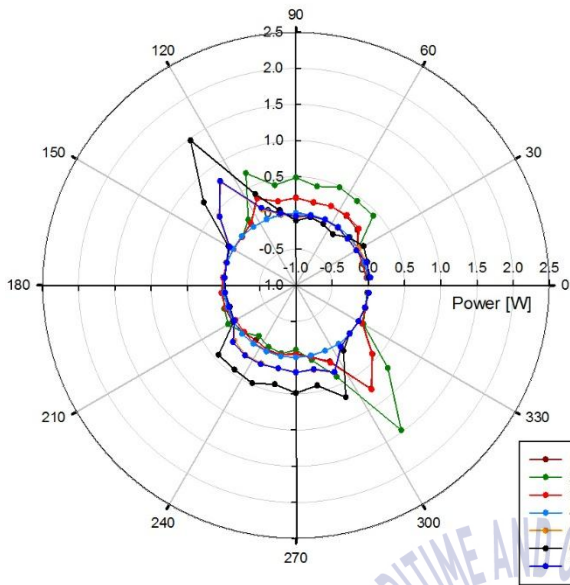
(b) 3/4 period of one cycle

Figure 18 Pressure contours in the flow field of the turbine domain at 1000rpm rotational speed and 2 sec period

Figure 19 indicates the power distribution on entire rotor. The divided power output was calculated by each torque of the runner blades during one cycle. Based on the center circle (zero), the outside lines represent the absorbed kinematic air energy by the rotor blades, and inner lines represent the energy loss due to turbulence and swirl of air at region 1 and 2. It is shown that the power output was commonly achieved at stage 1 for exhalation cycle and at stage 2 for inhalation cycle unlike power reduction and loss were observed in region 1 and 2. In addition, all different period have similar tendency of power distribution. The higher power output was acquired at shorter period as 1.25 sec, and the power amount was decreased as longer period.

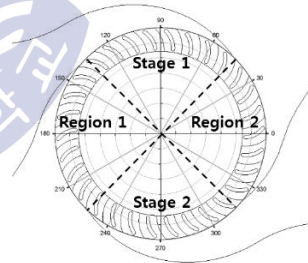
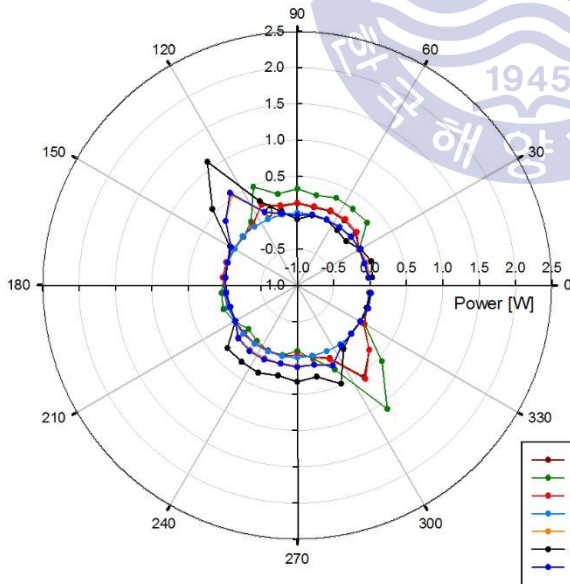


(a) 1.25 sec period



T6

(b) 1.5 sec period



T7

(c) 1.75 sec period

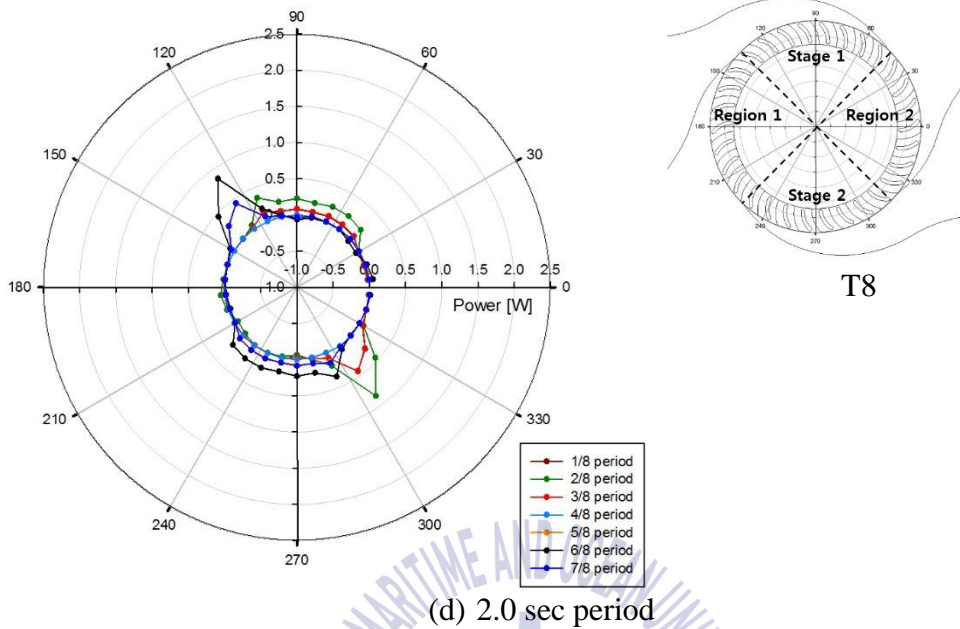
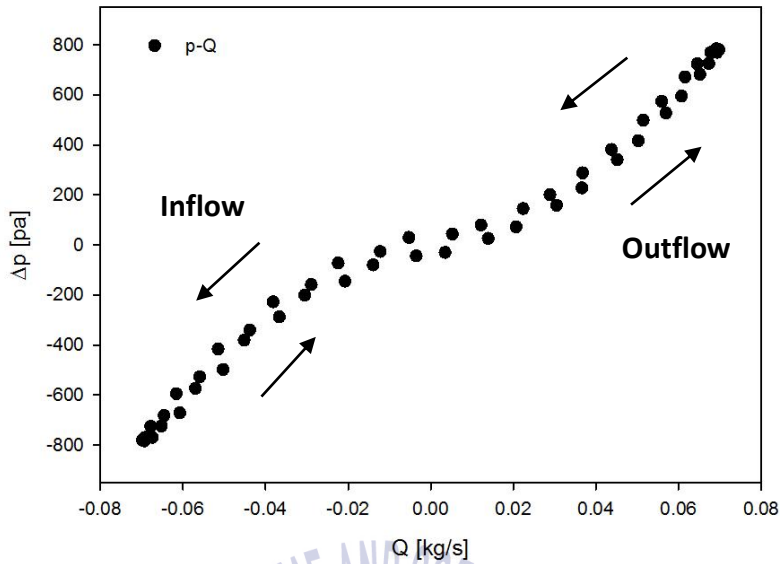
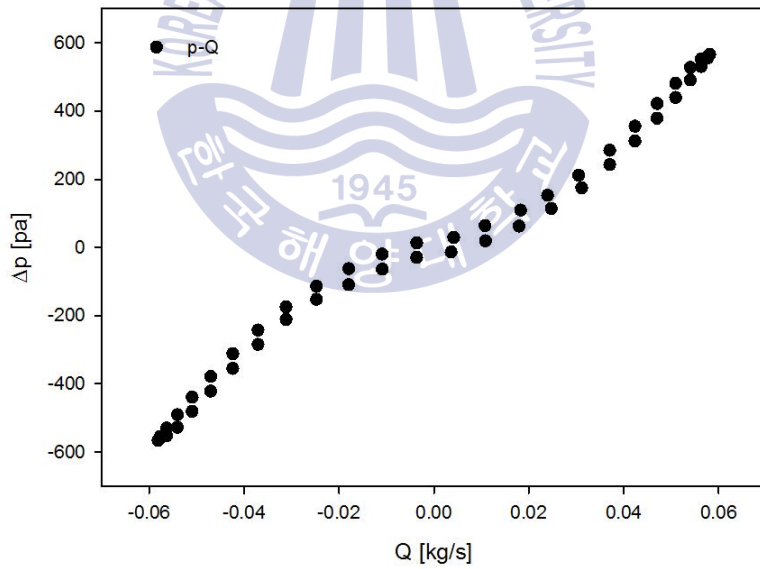


Figure 19 Power distribution on entire rotor at different wave periods

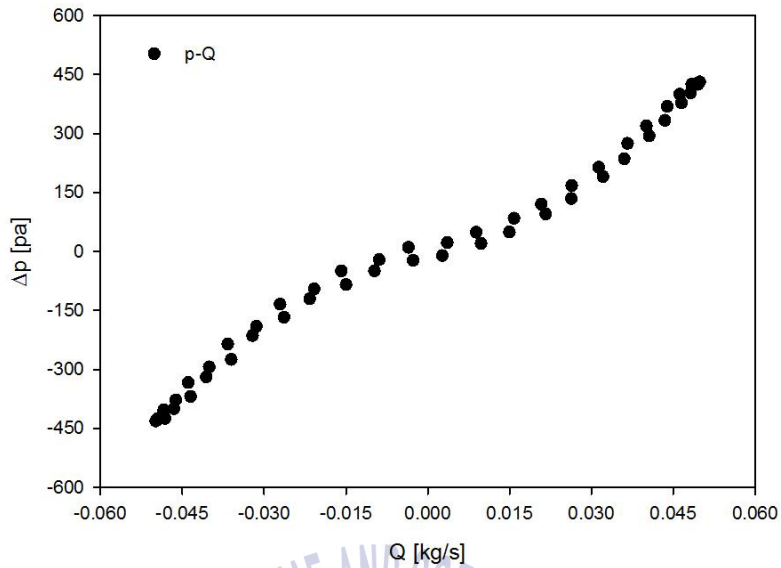
A relation between flow rate and pressure drop can be obtained as a hysteresis loop with the phase averaging method as shown in Figure 20. The hysteresis loop consists of exhalation and inhalation of the air flow, illustrated in (a) of Figure 20. The right side of the graph represents an exhalation of an air and the left side depicts an air inhalation. The gap between an increasing and decreasing lines for both outflow and inflow occurred due to the change of air density by the different air acceleration. For short period, at 1.25 sec, an irregular behavior in the hysteresis loop was obtained due to its significant effect of air compressibility. In addition, the pressure drop between upstream and downstream of the turbine becomes smaller as an increase of period, decrease the flow rate.



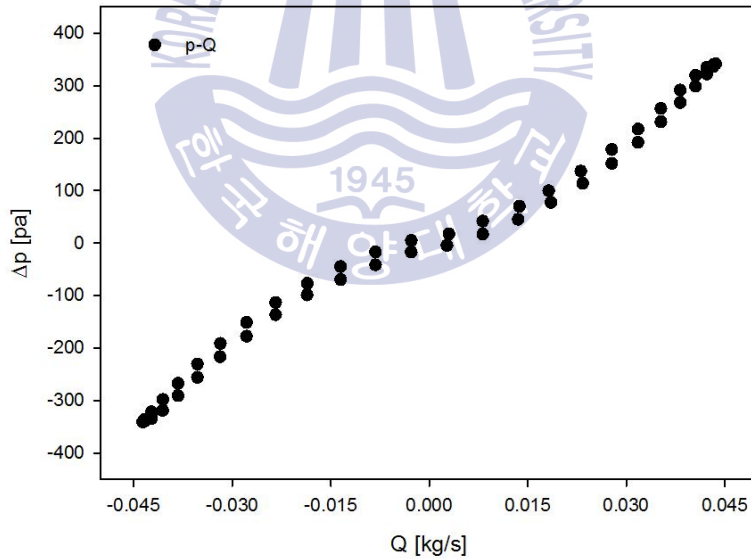
(a) 1.25 sec period



(b) 1.5 sec period



(c) 1.75 sec period



(d) 2.0 sec period

Figure 20 Pressure against flow rate with phase averaging at 1000rpm rotational speed

The time-series data of a torque on the turbine blade has been phase-averaged into one single phase as illustrated in Figure 21. The feature of the graphs for both exhalation and inhalation of the air flow have symmetrically same positive tendency since the blades are rotating uni-directional under the bi-directional flow condition. The peak torques for all cycle were acquired at the peak point of the pressure drop, which is increased proportional to the increase of pressure and flow rate.

With the phase averaged data of pressure, flow rate and torque, an aerodynamic power and turbine's shaft power can be obtained as shown in Figure 22. The feature of both air and shaft power graph have similar configuration as the torque graph. The air power represents the total amount of power which the air flow through the turbine have, and the shaft power represents the energy amount which turbine absorb from the aerodynamic power. As shown in the graphs, the power output is varying as time series. Thus, the averaged power output of air and shaft power was applied to calculate the averaged efficiency of the turbine performance. The summary of the turbine performance for different periods is illustrated in Table 8. The maximum efficiency of the turbine was 25.7% at 2.0 period and 1000 rpm rotational speed. The overall efficiency is around 23.6%

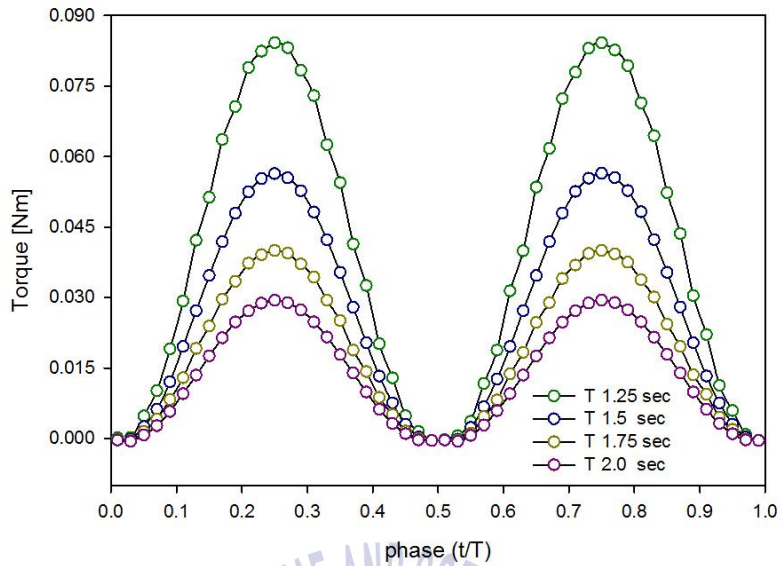
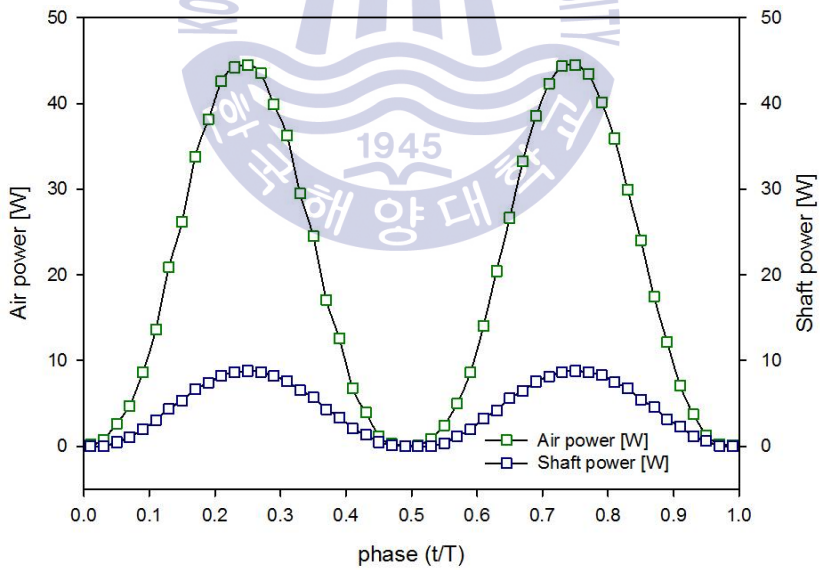
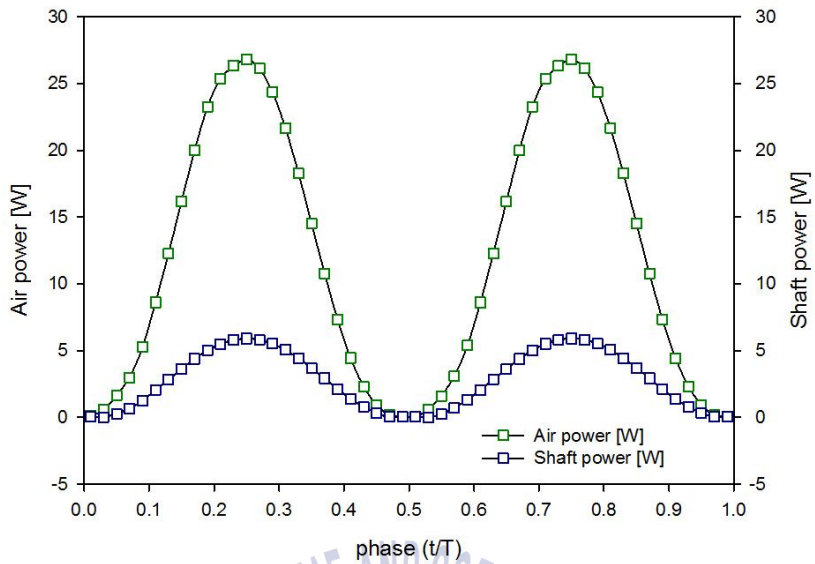


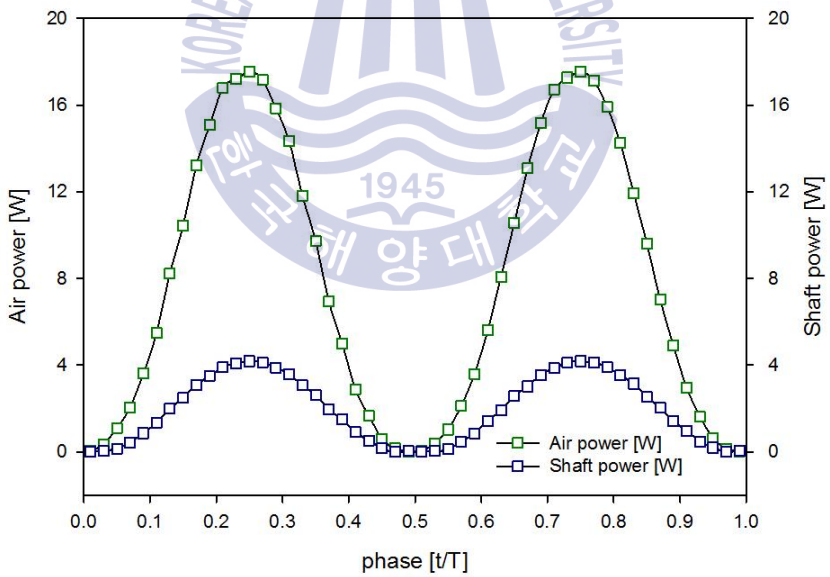
Figure 21 Representation of phase averaged times series cycles for turbine torque in one segment



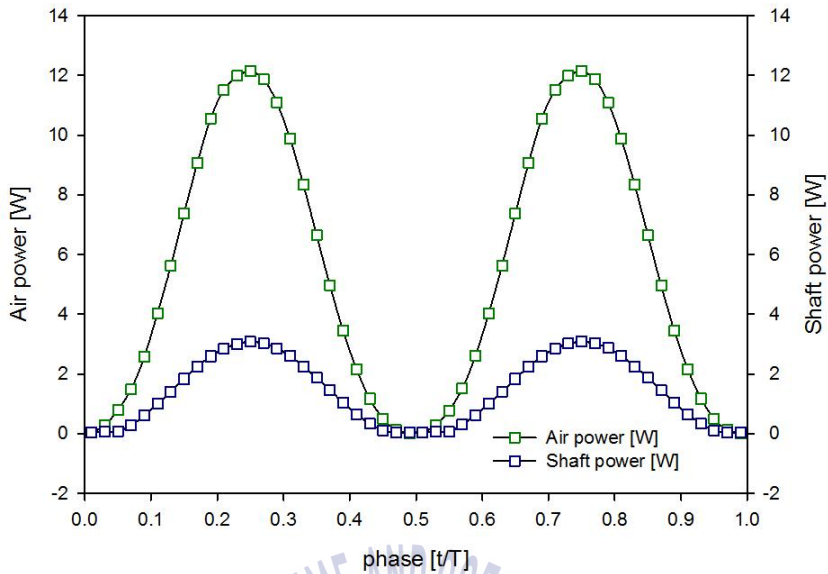
(a) 1.25 sec period



(b) 1.5 sec period



(c) 1.75 sec period



(d) 2.0 sec period

Figure 22 Phase averaged shaft power and air power

Table 8 Summary of performance of the model scaled cross-flow air turbine by CFD

Case		Averaged Data			
Period [sec]	Rotational Speed [rpm]	Torque [Nm]	Air power [W]	Shaft power [W]	Efficiency [-]
1.25	1000	0.040	19.87	4.20	0.211
1.5	1000	0.026	12.02	2.78	0.231
1.75	1000	0.019	7.90	1.95	0.246
2.0	1000	0.013	5.51	1.41	0.257

Chapter 3. Validation of an Orifice for turbine damping effects

The energy conversion process in OWC chamber produce a pressure drop across the chamber, which causes the oscillating amplitude of the water column. This in turn generates the cycle repeats and the pressure drops across the air turbine, which is the PTO device. However, it is difficult to install and investigate the model-scaled air turbine in the experiment due to the complexity of its geometric configuration and its relatively high rotational speed. Thus, the orifice plate is considered as a substitute of the air turbine for the investigation of similar behavior of pressure drop effects. In this section, the analysis of the turbine damping effects with the orifice plates for predicting the chamber performance by CFD and experiment will be discussed.

3.1 Ideal Air

In this section, several equations which are vital for the investigation of pressure – flow rate relationship will be discussed. The flow rate through an orifice is determined by calculation of the equations due to its difficulty of calibrating the oscillating flow rate. In addition, the flow rate equation contains the air compressibility. It is assumed that the air inside the chamber is isentropic for which a state equation for the open system can be represented in Equation (3.1), where absolute chamber pressure (P_c), chamber density (ρ_c) and specific heat ratio of the air ($\gamma = 1.4$).

$$\frac{P_c}{\rho_c^\gamma} = constant \quad (3.1)$$

Linearized expression for the density of air inside the chamber can be illustrated [26] as following Equation

$$\rho_c = \rho_0 \left(1 + \frac{p}{\gamma p_0} \right) \quad (3.2)$$

and

$$\frac{d\rho_c}{dt} = \frac{\rho_0}{\gamma p_0} \frac{dp}{dt} \quad (3.3)$$

Substituting Equation (3.2) and (3.3) into mass flow rate equation [26] results in Equation (3.4), where air mass (m) and changing chamber volume (V).

$$\frac{dm}{dt} = \rho_0 \left(1 + \frac{\rho_0}{\gamma p_0} \right) \frac{dV}{dt} + \frac{\rho_0 V}{\gamma p_0} \frac{dp}{dt} \quad (3.4)$$

A simplified expression of the air flow rate through the PTO system [27] can be described as shown in Equation (3.5), where initial chamber volume (V_0). The second term in the RHS of the equation is expressed as a modification due to the air compressibility [Sheng et al., 2013]. This equation will be used to calculate the flow rate through an orifice for both inflow and outflow due to its air compressibility and its simplicity, which can be easily applied in both inflow and outflow.

$$Q_p = -\frac{dV}{dt} - \frac{V_0}{\gamma p_0} \frac{dp}{dt} \quad (3.5)$$

3.2 Orifice PTO system

The most common equation of the volumetric flow rate through an orifice plate is derived from Bernoulli equation with several assumptions: the fluid is adiabatic and

frictionless, and the flow through the orifice is inviscid and turbulent [Kim and O'Neal, 1994] as shown in Equation (3.6), where a discharge coefficient (C_d) and cross-sectional area of the chamber (A).

$$Q = C_d A \sqrt{\frac{2\Delta p}{\rho}} \quad (3.6)$$

The air turbines such as impulse or Wells turbine for oscillating water column is a nonlinear PTO system [28]. The pressure drop through the turbine (the air chamber pressure) can be estimated as proportional to the flow rate squared. An orifice plate is commonly substituted for the simulation of nonlinear PTO system for the turbines due to its similar pressure effects during energy conversion [29]. The difference between exhalation and inhalation equations is due to the different flow direction. The positive sign represents the outflow from the air chamber, and the negative sign depicts the inflow from the atmosphere air.

3.3 Design of Orifice

The dimensions of the orifice plates were designed according to EN ISO standard [30]. The diameter ratio of the orifice, $\beta = d / D$, where d =orifice diameter and D =nozzle diameter, was calculated based on the cross-sectional area of the turbine nozzle. Various orifice plates with different orifice ratio were tested to obtain similar behavior of turbine damping effects, and the size of the orifice is $0.3D$ to $0.5D$ as shown in Table 9.

Table 9 Diameter ratio of test orifice plates

Diameter ratio	Dimensions
0.3D	40 mm
0.33D	44 mm
0.35D	47 mm
0.37D	50 mm
0.4D	54 mm
0.5D	67 mm

3.4 Numerical analysis of Orifice

The numerical analysis of orifice plates as a substitute for turbine damping effects under the sinusoidal air flow were conducted with same condition of previous turbine simulation. Various orifice plates with different diameter ratio were simulated to match the similar flow behavior of the turbine with pressure drop across the nozzle.

3.4.1 NUMERICAL ANALYSIS SETUP

The entire domain of the orifice plate have same model scale as the 1/16 scaled turbine, and it was analyzed excluding the OWC chamber and wave motion as well as depicted in Figure 24. The mesh comprising fine hexahedral grids with 1.51×10^6 nodes was generated as shown in Figure 23. The transient type of simulation was applied so that same bi-directional sinusoidal flow can pass through the orifice, which generate the damping effects. The same condition of sinusoidal air flow as the turbine was adopted in order to compare the result under same flow condition.

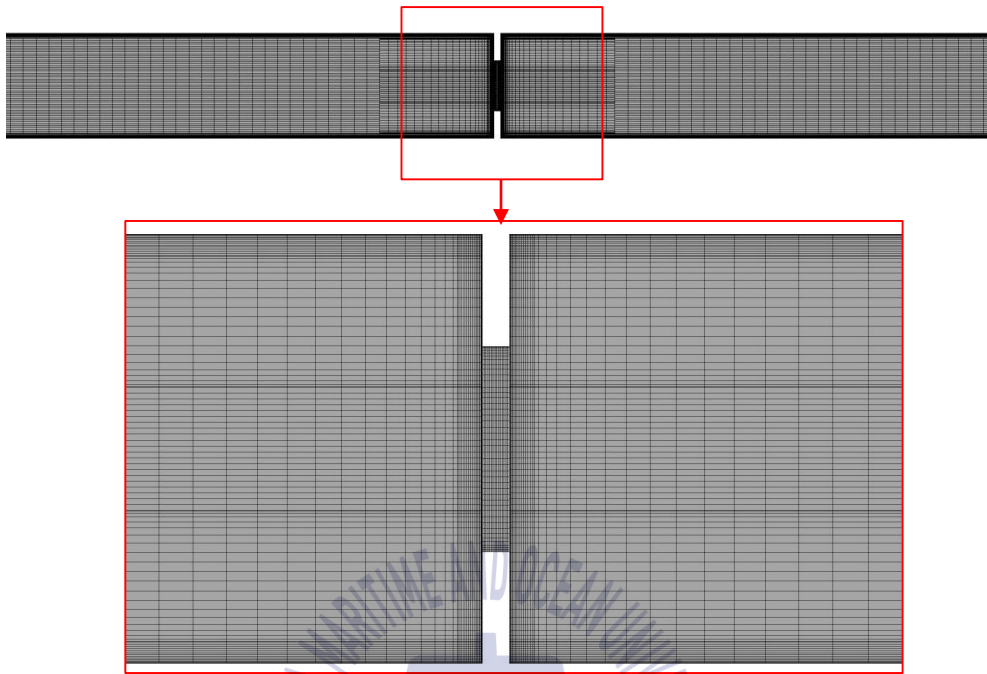


Figure 23 Meshing of the orifice plate by ICEM CFD

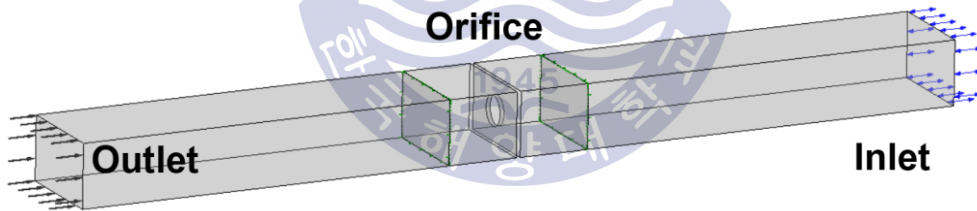
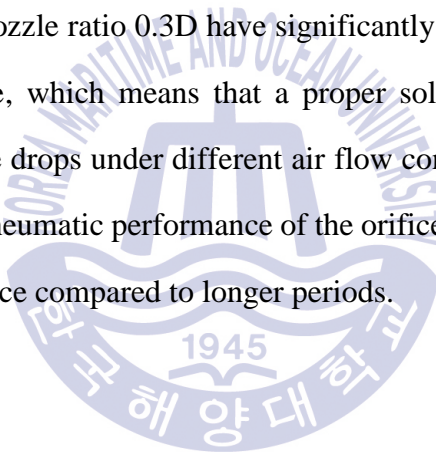
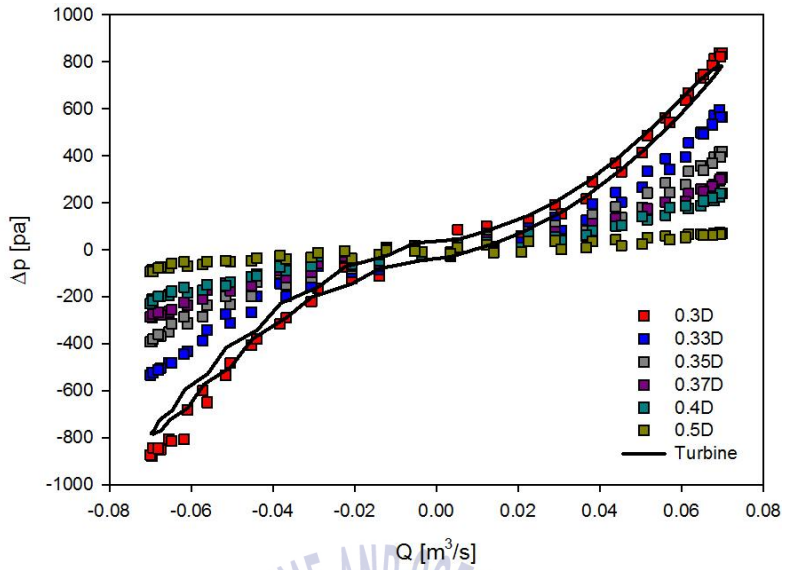


Figure 24 Configuration of CFX pre setup domain for the orifice plate in transient simulation

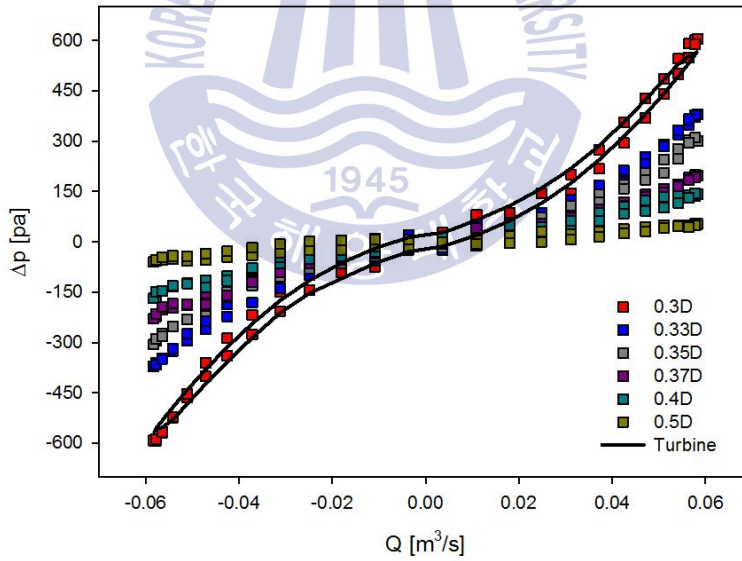
3.4.2 CFD RESULT AND DISCUSSION

CFD simulation under the bi-directional flow for the pressure effects for the orifice plate as a substitute has been carried out. It can be seen that the pressure drop across the upstream and downstream of the orifice plate have a similar behavior of the turbine damping effects. Varying the diameter ratio of the orifice induced the different pressure drop under same flow rate condition. The entire phase-averaged data of pressure and flow rate diagram was depicted in Figure 25. The smaller size of the orifice diameter caused the increase of the pressure drop across the orifice. It was indicated that the nozzle ratio 0.3D have significantly closer fitting behavior to the turbine performance, which means that a proper solidity of the orifice plate induced similar pressure drops under different air flow conditions. For short period of sinusoidal flow the pneumatic performance of the orifice was relatively less fitted to the turbine performance compared to longer periods.

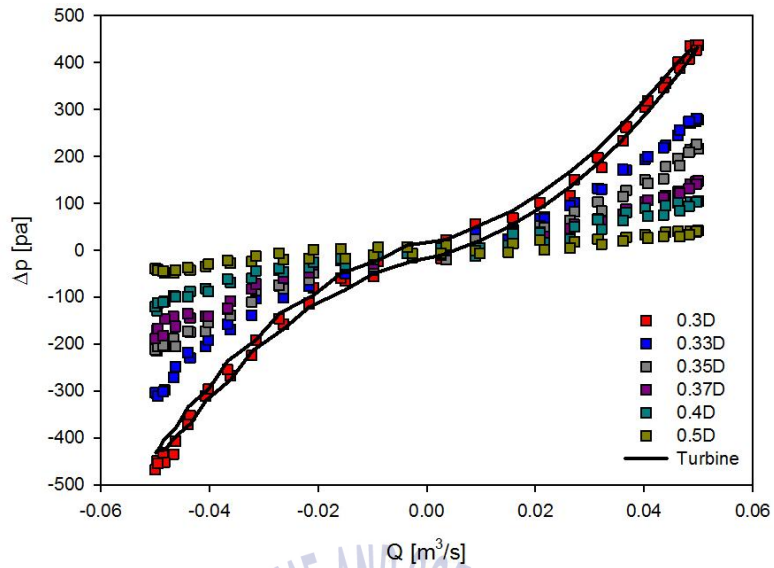




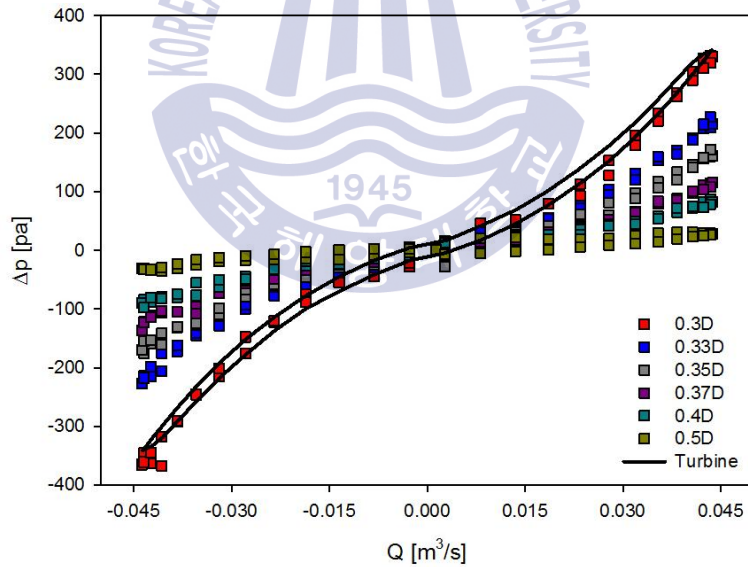
(a) 1.25 sec period



(b) 1.5 sec period



(c) 1.75 sec period



(d) 2.0 sec period

Figure 25 Phase averaged pressure drop and flow rate diagram of the orifice plates with the turbine result

3.5 Experimental analysis of Orifice

The experiment was designed and conducted at experiment facility of Korea Maritime and Ocean University to validate the result of CFD numerical analysis with the experimental result, which represents a real flow behavior. To generate the turbine damping effect through the nozzle, the 1/16 scaled OWC chamber was adopted into the wave tank. The orifice plate as the turbine substitute was then installed inside the nozzle of the OWC chamber. The boundary conditions (wave heights and periods) to generate the same condition of bi-directional flow into the orifice were designed equally.

Model scale experimentation introduces an opportunity to investigate the non-linear phenomena of the wave energy converter' performance [25]. In this section, the model scale experiment of OWC air chamber with the orifice plates will be discussed. Several assumptions are established to achieve simplicity of analysis and relevant result as follows:

- The air is considered as an ideal gas [31]
- The transformation is considered adiabatic
- The air pressure and temperature are considered homogeneous within the chamber [32]
- Air velocities and pressure are uniform over the cross sectional area [33]

The orifice plates were installed at the nozzle of the OWC chamber as shown in Figure 26. The OWC chamber installed in the wave tank, illustrated in Figure 27 and Figure 28, faces the oncoming wave, generated by the piston type wave maker. The

OWC chamber model is composed of Acrylic material with its thickness of 10mm so that the wave behavior can be observed. The design wave was fixed as 0.125m with 1.25 to 2.0 sec of periods. The diameter ratio of the orifice plates (0.3D, 0.33D, 0.35D, 0.37D, 0.4D) were tested.

The two ultrasonic wave height meters were installed in 1m front of and at the top of the OWC chamber to measure the height of oncoming wave and inside the chamber respectively. The measured wave height then is transmitted into the wave meter transducer, which deliver the signal to a data logger. In addition, the averaged pressure at the upstream and downstream of the orifice plate is measured by a pressure sensor as shown in Figure 29.

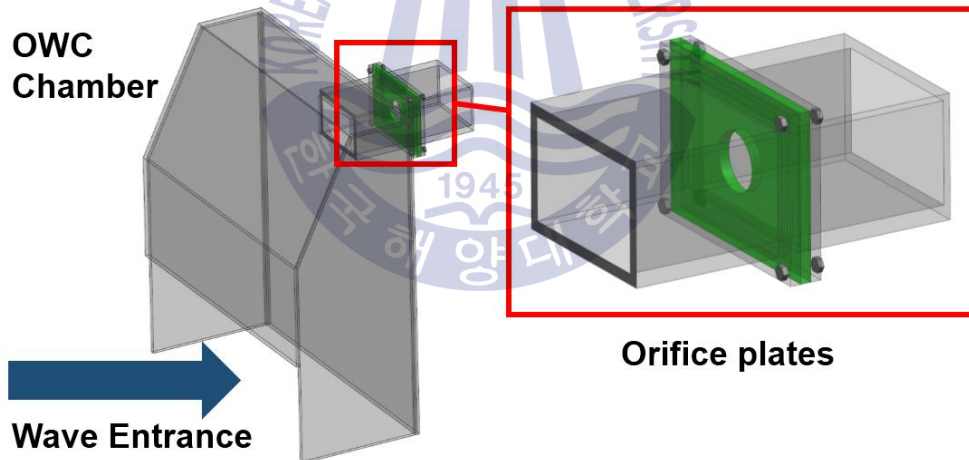


Figure 26 Configuration of OWC chamber with orifice plates

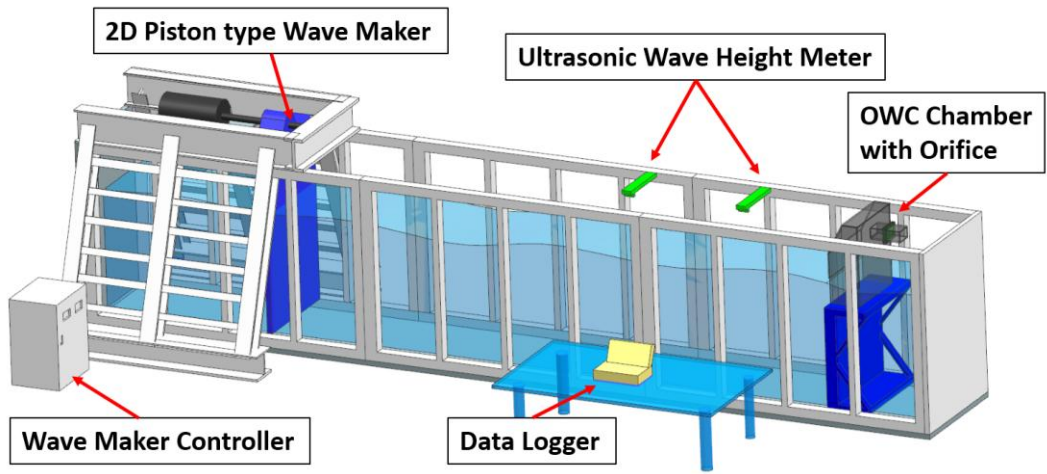


Figure 27 Configuration of experimental setup in wave tank

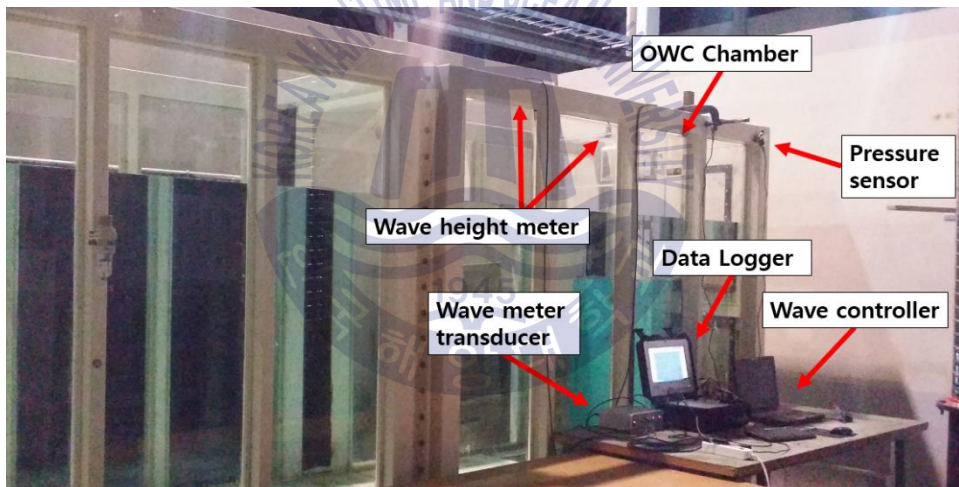
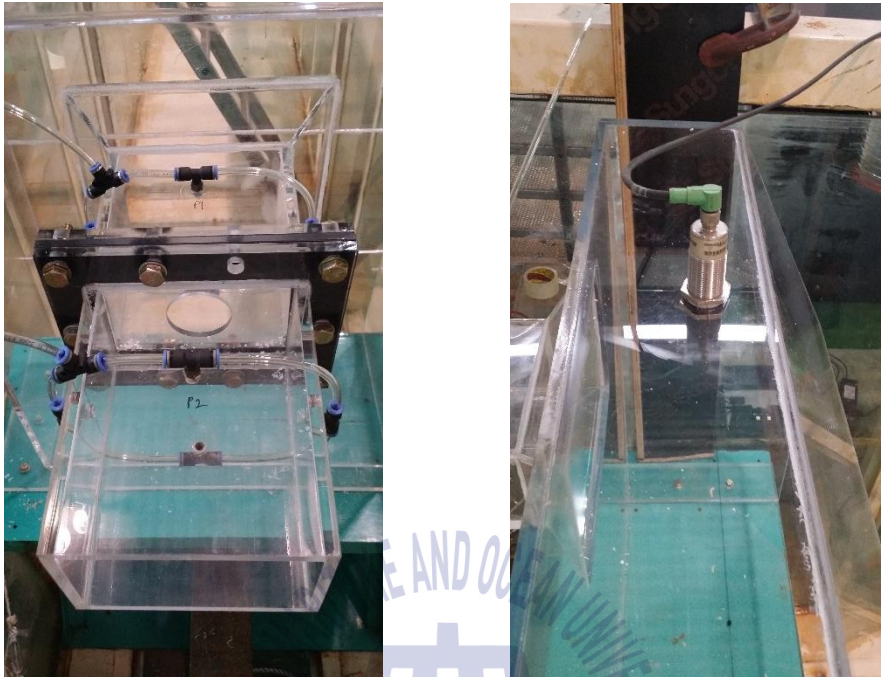


Figure 28 Experimental setup with OWC chamber in wave tank



(a) pressure sensor setup

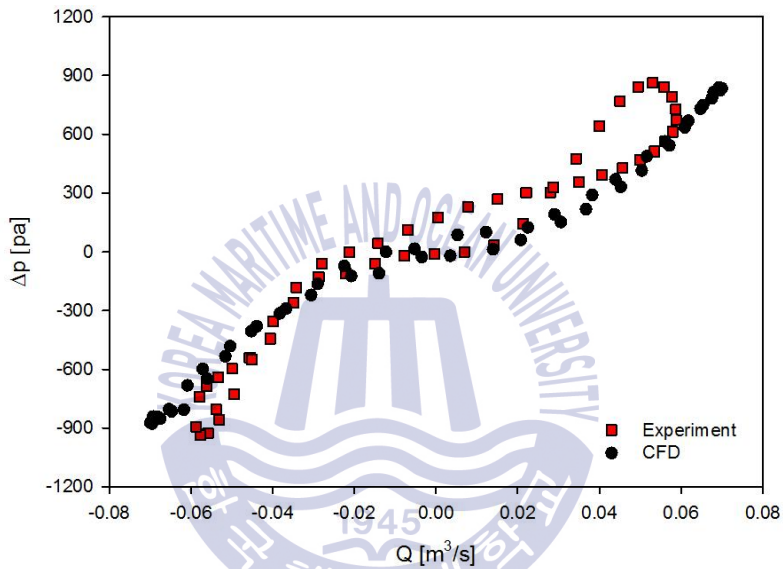
(b) wave height meter setup

Figure 29 Experimental equipment in OWC chamber for measurement

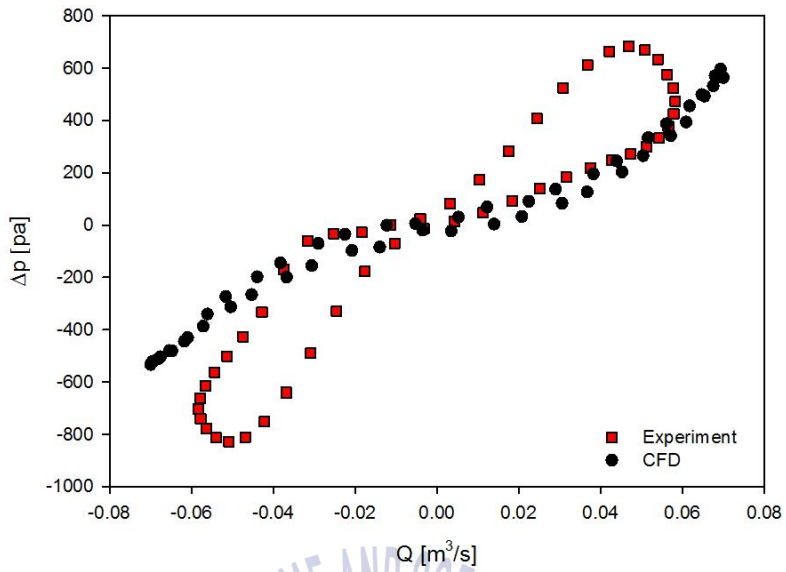
3.6 Result of experiment and comparative study

The validation of the orifice plate embedded in the OWC chamber was processed at the condition of 0.125m wave height and 1.25 sec wave period. Its significant wave reflection in longer periods due to relatively small size of wave tank decrease the design wave height inside the water chamber and wave tank, which cause a difficulty of making design wave height at longer wave periods. Figure 30 presents the comparison in pressure and flow rate diagram between CFD simulations and experiment at the 1.25 sec period with 0.3D, 0.33D, 0.35D, 0.37D and 0.4D size orifices. It can be seen that the pneumatic power in orifice plates by CFD is considerably fitted to the performance of the orifice by experiment. The 0.3D orifice

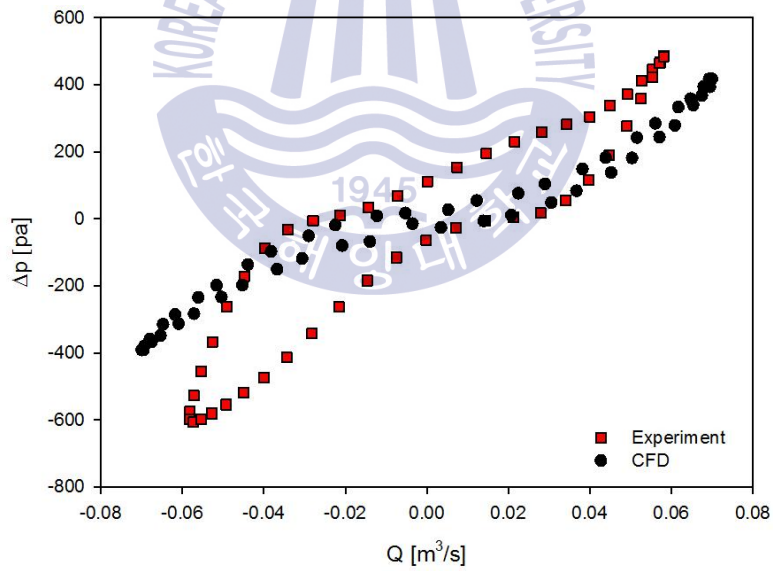
size, which is fitted to the pressure drop of turbine, have the closest behavior as the experiment compared to other sizes. The pressure drop across the orifice and flow rates have relatively irregular features due to irregular motion of waves inside the chamber and air compressibility.



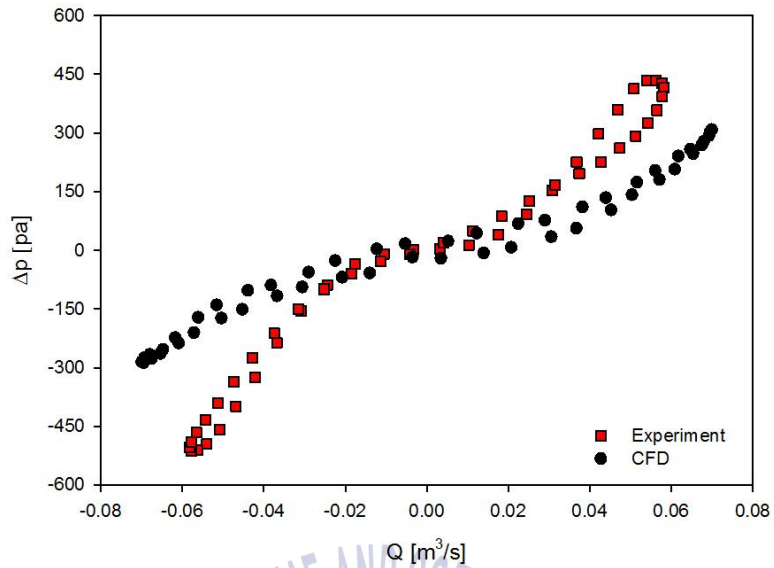
(a) Orifice 0.3D and 1.25 sec period



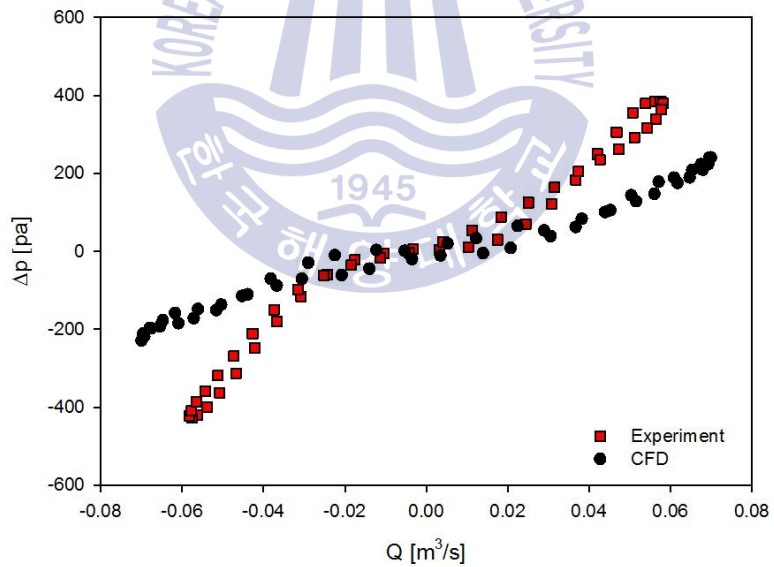
(b) Orifice 0.33D and 1.25 sec period



(c) Orifice 0.35D and 1.25 sec period



(d) Orifice 0.37D and 1.25 sec period



(e) Orifice 0.4D and 1.25 sec period

Figure 30 Validations of orifice plate as substitute for the cross-flow air turbine between CFD and experiment result

Chapter 4. Conclusion

The study of the cross-flow air turbine for OWC wave energy converter have been processed. The cross-flow air turbine have a potential strengths such as low speed of rotational speed at wider range of flow condition compared to other types of air turbines for OWCs, which may provide low level of noise during its operation. However, the technology of the cross-flow air turbine is an early stage of development, and it has significant tasks (relatively low performance efficiency as 25% peak efficiency) which should be settled. The enhancement of the turbine performance in further study could provide another competitive option of air turbine for OWC wave energy converter.

The preliminarily study of the cross-flow air turbine for its performance analysis have been carried out by CFD. The highest efficiency of the turbine was 58.7% at the rotational speed of 48 rpm and the inlet velocity of 12m/s under uni-directional flow condition. All performance for different rotational speed have relatively same tendency and its performance curves tend to significantly drop after the stall region. It means that the operating range of the turbine have relatively low range. It should be enhanced by further geometrical modification or possible variables.

It is vital to consider the turbine damping effects for investigation of OWC air chamber. Due to its complex configuration and high rotational speed of model scaled air turbine, there is a difficulty of installing the model scaled turbine on the OWC air chamber. Therefore, the numerical analysis of the turbine by CFD and investigation of orifice plates by CFD and experiment to validate the substitutability of orifice

plates have been proposed. The 1/16 model scale for turbine and orifice was determined to be fit to the experiment facilities. From the CFD and experiment analysis, it was found that the 0.3D can generate pressure drops identical to the cross-flow air turbine and it had a considerably similar behavior to the orifice performance by experiment. It can be concluded that the verification of the CFD result with the experiment result is achieved relatively well although the experiment at longer wave periods were not proposed due to the inadequacy in experiment facilities' capacity.



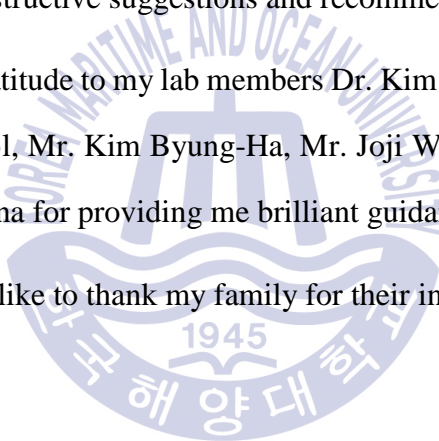
Acknowledgements

First of all, I deeply appreciate my supervisor Prof. Lee Young-Ho who provided me the invaluable advices and recommendations during 2 years for the master's degree. Thanks to the supports, I was able not only to finish my thesis but also to have priceless experience.

I am also grateful to the thesis committee, Prof. Yoon Hyung-Kee (Chairperson, Review Panel) and Dr. Hwang Tae-Gyu (Co-Chairperson) for their thumping encouragement and constructive suggestions and recommendations.

I have my heartfelt gratitude to my lab members Dr. Kim Chang-Goo, Mr. Park Ji-Hoon, Mr. Kim In-Cheol, Mr. Kim Byung-Ha, Mr. Joji Wata, Mr. Jeong Hui-Song and Mr. Ayham Habashna for providing me brilliant guidance and support.

Additionally, I would like to thank my family for their infinite and priceless love.



Reference

- [1] Muetze, A. and Vining, J.G., 2006. October. Ocean wave energy conversion-a survey. *In Conference Record of the 2006 IEEE Industry Applications Conference Forty-First IAS Annual Meeting* (Vol. 3, pp. 1410-1417). IEEE.
- [2] Richard Boud, 2003. "Status and Research and Development Priorities, Wave and Marine Accessed Energy," UK Dept. of Trade and Industry (DTI), DTI Report # FES-R-132, AEAT Report # AEAT/ENV/1054, United Kingdom
- [3] Wavemill Energy Corp., "Electric power form ocean waves", [Online] Available: <http://www.wavemill.com>
- [4] The Executive Committee of Ocean Energy Systems, 2015. OES annual report 2015. IEA-OES.
- [5] SI OCEAN, 2014. Ocean Energy: State of the Art
- [6] Wave Dragon company, 2015 [Online] Available: <http://www.wavedragon.net/>
- [7] EMEC, 2012. "EMEC to support development of South Korean Marine Energy Centre". The European Marine Energy Centre LTD [Online] Available:<http://www.emec.org.uk/emec-to-support-development-of-south-korean-marine-energy-centre/>
- [8] Voith company website, 2015. [Online] Available: <http://www.voith.com/>
- [9] Masuda, Y., and Muyazaki, T., 1979. Wave power electric generation study in Japan. *Int. Symposium on Wave and Tidal Energy*, British Hydromechanics Research Association Fluid Engineering, Cranfield, Beds., England

- [10] Hotta, H., Miyazaki, T., Washino, Y., and Ishii, S., 1988. On the performance of the wave power device Kaimei-The results on the open sea tests. *Proc., 7th Int. Offshore and Polar Engineering Conf.*, ISOPE, Houston, 91-96
- [11] Sheng, W., Lewis, T., and Alcorn, R., 2012. On wave energy extraction of oscillating water column device. *4th International Conference on Ocean Energy*.
- [12] Sarmiento, A. J. N. A., Gato, L. M. C. and de O. Falcao, A. F., 1990. Turbine-controlled wave energy absorption by oscillating water column devices, *Ocean Engineering*, Vol. 17, pp: 481-497
- [13] SHENG, W., ALCORN, R. & LEWIS, A., 2013. On thermodynamics in the primary power conversion of oscillating water column wave energy converters. *Journal of Renewable and Sustainable Energy*, 5, 023105.
- [14] Sheng, W., Thiebaut, F., Babuchon, M., Brooks, J., Alcorn, R. and Lewis, A., 2013. Investigation to air compressibility of oscillating water column wave energy converters, *Proceedings of the ASME 2013 32nd International Conference in Ocean, Offshore and Arctic Engineering, OMAE 2013*, 9-14th June, 2012, Nantes, France
- [15] Lindsley, E. F., 1977. "Water power for your home", *popular science*, vol. 210, no. 5, pp. 87-93
- [16] Mockmore, C. A. and Merryfield, Fred., 1949. *The Banki Water Turbine*. Engineering Experiment Station Oregon State system of Higher Education Oregon State College Corvallis.

- [17] FUKUTOMI, J., NAKASE, Y. and Watanabe, T., 1985. A numerical method of free jet from a cross-flow turbine nozzle. *Bulletin of JSME*, 28(241), pp.1436-1440.
- [18] Akabane, M., Suzuki, H. and Yamauchi, K., 1984. On the cross flow turbine for wave power plant. *In Proceedings of the 1st Symposium on wave energy utilization in Japan*.
- [19] Hudspeth, R.T., 2006. Waves and wave forces on coastal and ocean structures, Vol. 21. World scientific.
- [20] McCormick, M. E., 2013. Ocean wave energy conversion. Courier Corporation.
- [21] Demirbilek, Z. and Vincent, C., 2002. Water Wave Mechanics Coastal Engineering Manual. EM 1110-2-1100. US Army Corps of Engineers, USA.
- [22] ANSYS-CFX ver. 14 Manual, 2010, ANSYS
- [23] Versteeg, H.K. and Malalasekera, W., 2007. An introduction to computational fluid dynamics: the finite volume method. Pearson Education.
- [24] Falcao, AFO. And Gato, LMC., 2012. 8.05 Air turbines. *Comprehensive Renewable Energy*, Vol. 8. doi: 10.1016/B978-0-08-087872-0.00805-2
- [25] FLEMING, A., PENESIS, I., MACFARLANE, G., BOSE, N. & HUNTER, S., 2012. Phase averaging of the velocity fields in an oscillating water column using splines. *Proceedings of the Institution of Mechanical Engineers, Part M: Journal of Engineering for the Maritime Environment*, 226, 335-345.

[26] SHENG, W., ALCORN, R. & LEWIS, A., 2013. On thermodynamics in the primary power conversion of oscillating water column wave energy converters. *Journal of Renewable and Sustainable Energy*, 5, 023105.

[27] SARMENTO, A. J. & FALCÃO, A. D. O., 1985. Wave generation by an oscillating surface-pressure and its application in wave-energy extraction. *Journal of Fluid Mechanics*, 150, 467-485.

[28] ANAND, S., JAYASHANKAR, V., NAGATA, S., TOYOTA, K., TAKAO, M. & SETOGUCHI, T., 2007. Performance estimation of bi-directional turbines in wave energy plants. *Journal of Thermal Science*, 16, 346-352.

[29] Dizadji N, Sajadian S E., 2011. Modeling and optimization of the chamber of OWC system. *Energy*, 36: 2360-2366

[30] ISO, E. 5167-2: 2003. Measurement of Fluid Flow by Means of Pressure Differential Devices Inserted in Circular-Cross Section Conduits Running Full-Part, 2.

[31] F. THIEBAUT, J. G., A. PELLAT, D. O'SULLIVAN AND R. ALCORN, 2010. Servomotor controlled piston rig for the simulation of an Oscillating Water Column air chamber. 3rd International Conference on Ocean Energy.

[32] FORESTIER, J., HOLMES, B., BARRETT, S. & LEWIS, A., 2007. Value and validation of small scale physical model tests of floating wave energy converters. European Wave and Tidal Energy Conference.

[33] GROß, F. P. T. F., 2010. Flow rate measurement by an orifice in a slowly reciprocating gas flow. *Flow Measurement and Instrumentation*, 22, 81-85.